

ICES REPORT 15-12

April 2015

Isogeometric Analysis of Boundary Integral Equations

by

Matthias Taus, Gregory J. Rodin and Thomas J. R. Hughes



The Institute for Computational Engineering and Sciences
The University of Texas at Austin
Austin, Texas 78712

Reference: Matthias Taus, Gregory J. Rodin and Thomas J. R. Hughes, "Isogeometric Analysis of Boundary Integral Equations," ICES REPORT 15-12, The Institute for Computational Engineering and Sciences, The University of Texas at Austin, April 2015.

Report Documentation Page				Form Approved OMB No. 0704-0188	
Public reporting burden for the collection of information is estimated to average 1 hour per response, including the time for reviewing instructions, searching existing data sources, gathering and maintaining the data needed, and completing and reviewing the collection of information. Send comments regarding this burden estimate or any other aspect of this collection of information, including suggestions for reducing this burden, to Washington Headquarters Services, Directorate for Information Operations and Reports, 1215 Jefferson Davis Highway, Suite 1204, Arlington VA 22202-4302. Respondents should be aware that notwithstanding any other provision of law, no person shall be subject to a penalty for failing to comply with a collection of information if it does not display a currently valid OMB control number.					
1. REPORT DATE 21 APR 2015		2. REPORT TYPE		3. DATES COVERED 00-00-2015 to 00-00-2015	
4. TITLE AND SUBTITLE Isogeometric Analysis of Boundary Integral Equations				5a. CONTRACT NUMBER	
				5b. GRANT NUMBER	
				5c. PROGRAM ELEMENT NUMBER	
6. AUTHOR(S)				5d. PROJECT NUMBER	
				5e. TASK NUMBER	
				5f. WORK UNIT NUMBER	
7. PERFORMING ORGANIZATION NAME(S) AND ADDRESS(ES) University of Texas at Austin, Institute for Computational Engineering and Sciences, Austin, TX, 78712				8. PERFORMING ORGANIZATION REPORT NUMBER	
9. SPONSORING/MONITORING AGENCY NAME(S) AND ADDRESS(ES)				10. SPONSOR/MONITOR'S ACRONYM(S)	
				11. SPONSOR/MONITOR'S REPORT NUMBER(S)	
12. DISTRIBUTION/AVAILABILITY STATEMENT Approved for public release; distribution unlimited					
13. SUPPLEMENTARY NOTES					
14. ABSTRACT Isogeometric analysis is applied to boundary integral equations corresponding to boundary-value problems governed by Laplace's equation. It is shown that the smoothness of geometric parametrizations central to computer-aided design can be exploited for regularizing integral operators. As a result one obtains high-order collocation methods based on superior approximation and numerical integration schemes and well-conditioned systems of linear algebraic equations. It is demonstrated that the proposed approach allows one to solve boundary-value problems with an accuracy close to machine precision.					
15. SUBJECT TERMS					
16. SECURITY CLASSIFICATION OF:			17. LIMITATION OF ABSTRACT Same as Report (SAR)	18. NUMBER OF PAGES 31	19a. NAME OF RESPONSIBLE PERSON
a. REPORT unclassified	b. ABSTRACT unclassified	c. THIS PAGE unclassified			

Isogeometric Analysis of Boundary Integral Equations

Matthias Taus, Gregory J. Rodin and Thomas J. R. Hughes

*Institute for Computational Engineering and Sciences
University of Texas at Austin
Austin, TX 78712 USA*

April 21, 2015

Abstract

Isogeometric analysis is applied to boundary integral equations corresponding to boundary-value problems governed by Laplace’s equation. It is shown that the smoothness of geometric parametrizations central to computer-aided design can be exploited for regularizing integral operators. As a result, one obtains high-order collocation methods based on superior approximation and numerical integration schemes and well-conditioned systems of linear algebraic equations. It is demonstrated that the proposed approach allows one to solve boundary-value problems with an accuracy close to machine precision.

1 Introduction

Isogeometric analysis (IgA) [24, 35] is a framework for numerical schemes for solving boundary-value problems (BVPs) in which the basis functions coincide with those used for geometric parametrizations in computer aided design (CAD). Thus, in contrast to conventional finite element methods, IgA relies on Non-Uniform Rational B-splines (NURBS) [43, 46], T-splines [55, 53] or subdivision surfaces [21, 48, 51] rather than piecewise polynomials as the basis functions. IgA simplifies mesh generation, and thus it significantly shortens the design-through-analysis process for high-end engineering components. Furthermore, IgA is advantageous because, in contrast to finite element methods, it fully preserves geometry of CAD-generated shapes and involves basis functions with attractive properties. These features have given rise to accurate and efficient numerical schemes successfully applied to fluid mechanics [1, 3, 5, 7, 8, 12, 29], solid mechanics [39], electromagnetism [20], fluid-structure interaction [9, 10, 11, 60], structural dynamics [25, 26], plates and shells [15, 16, 27, 28, 37, 22, 23], phase-field models [17, 32, 33], and shape optimization [40, 41, 45, 59].

Boundary element methods (BEMs) are numerical schemes for solving boundary integral equations (BIEs). Like finite element methods, BEMs rely on piecewise polynomials for approximating the geometry and field variables. Thus, by replacing piecewise polynomials with NURBS or T-splines, one can develop isogeometric BEMs. This approach has been already undertaken [13, 14, 31, 38, 42, 44, 54, 56].

The premise of this paper is that IgA can radically improve numerical schemes for solving BIEs because of the additional smoothness of NURBS and T-splines in comparison to C^0 -continuous piecewise polynomials. We show that one can regularize the key singular integral operators, and construct superior approximation and integration schemes and well-conditioned systems of linear algebraic equations. These schemes allow one to solve BIEs with machine precision. We demonstrate these advantages of IgA by applying it to BIEs corresponding to Laplace’s equation. This restriction significantly simplifies mathematical aspects of our work, but most of the results can be readily extended to equations of classical elasticity and Stokes equations of fluid mechanics.

In the context of BEMs, the proposed approach can be classified as a high-order collocation method allowing for weakly-singular, singular, and hyper-singular integral operators. Previously this setting was possible with Galerkin but not collocation methods. Accordingly, we exploited analytical tools different from those usually used in analysis of Galerkin methods [49, 58]. In this regard, we believe that our approach may be useful for developing mathematical foundations for collocation schemes for BIEs. In addition, collocation BEMs dominate engineering applications, thus we believe that our results are not only of mathematical but also practical interest.

The rest of the paper is organized as follows. In Section 2, we define the model BVP, corresponding BIEs, and a proper continuous setting for BVPs defined on domains with smooth boundaries. In Section 3, we introduce collocation schemes for the integral operators, defined on smooth surfaces. In Section 4, we demonstrate that all collocated integral operators defined on smooth surfaces can be reduced to weakly-singular integrals. In Section 5, we briefly summarize basic results from IgA and identify extensions needed for solving BIEs. We also describe the extension of our methodology to piecewise smooth surfaces which allows us to accommodate multiple patches with C^0 -continuity, degenerate patches resulting in local C^0 -continuity, and extraordinary points or star-points. In Section 6, we consider representative example problems, which allow us to demonstrate various important mathematical and computational aspects. In Section 7, we summarize key results of this work and briefly discuss directions for future research. Mathematical details are presented in the appendix.

2 Continuous Formulation

2.1 Model boundary-value problem

Consider a bounded domain $\Omega \subset \mathbb{R}^3$ with $\Gamma := \partial\Omega$. We assume that Γ is a C^2 -surface ($\Gamma \in C^2$), which, loosely, means that Γ can be mapped on \mathbb{R}^2 , and the inverse of that map ψ is twice continuously differentiable. For a rigorous definition of C^2 -surfaces we refer to the appendix. This restriction $\Gamma \in C^2$ is sufficient for establishing mathematical foundations for integral equations. A typical CAD parametrization map can be defined as a union of C^2 -surfaces, resulting in a globally Lipschitz Γ ; we denote this class of surfaces by \tilde{C}^2 . Unfortunately, mathematical foundations for BIEs defined on \tilde{C}^2 -surfaces are not well developed at this stage. Thus, in this and two following sections, we restrict our attention to $\Gamma \in C^2$. On the other hand, the loss of smoothness of \tilde{C}^2 -surfaces can be compensated by using appropriate numerical schemes presented in Sections 5 and 6.

The model BVP is formulated for Laplace's equation

$$-\Delta u = 0 \quad \text{in } \Omega, \tag{1}$$

and mixed boundary conditions, which include Dirichlet

$$u = g_D \quad \text{on } \Gamma_D, \tag{2}$$

and Neumann

$$t := n \cdot \nabla u = g_N \quad \text{on } \Gamma_N \tag{3}$$

data. Here n denotes the outward unit normal vector on Γ ; $\overline{\Gamma_D \cup \Gamma_N} = \Gamma$ and $\Gamma_D \cap \Gamma_N = \emptyset$. At this stage, we require $\Gamma \in C^2$, but we do not specify the smoothness of u , g_D , and g_N . This will be done once we introduce the integral operators.

2.2 Integral equations

The integral equations equivalent to (1)-(3) and their mathematical properties are well known [34, 49, 58]. They involve the representation formula that allows one to determine the solution u in terms of the Cauchy boundary data (u, t) :

$$u(x) = \int_{\Gamma} G(x, y) t(y) ds_y - \int_{\Gamma} n(y) \cdot [\nabla_y G(x, y)] u(y) ds_y \quad x \in \Omega, \quad (4)$$

where

$$G(x, y) = \frac{1}{4\pi|x - y|}$$

is the fundamental solution of Laplace's equation. The Cauchy data can be reconstructed using the singular boundary integral equation (SBIE)

$$\left(\frac{1}{2}\mathcal{I} + \mathcal{K}\right)u = \mathcal{V}t \quad \text{on } \Gamma.$$

Here \mathcal{I} is the identity,

$$\mathcal{V}t(x) := \int_{\Gamma} G(x, y) t(y) ds_y, \quad x \in \Gamma$$

is the single-layer operator, and

$$\mathcal{K}u(x) := \int_{\Gamma} n(y) \cdot [\nabla_y G(x, y)] u(y) ds_y, \quad x \in \Gamma$$

is the double-layer operator. Alternatively, the Cauchy data can be reconstructed using the hyper-singular integral equation (HSBIE)

$$\left(\frac{1}{2}\mathcal{I} - \mathcal{K}'\right)t = \mathcal{D}u \quad \text{on } \Gamma,$$

where

$$\mathcal{K}'t(x) := \int_{\Gamma} n(x) \cdot [\nabla_x G(x, y)] t(y) ds_y, \quad x \in \Gamma$$

is the adjoint double-layer operator, and

$$\mathcal{D}u(x) := - \int_{\Gamma} n(x) \cdot \{\nabla_x n(y) \cdot [\nabla_y G(x, y)]\} u(y) ds_y, \quad x \in \Gamma$$

is the hyper-singular operator.

2.3 Analysis of integral equations

Since $\Gamma \in C^2$ one can prove that the operators

$$\mathcal{K}, \mathcal{K}' : C(\Gamma) \rightarrow C(\Gamma)$$

are compact; see Appendix. Here $C(\Gamma)$ is the space of continuous functions on Γ . Similarly, we adopt the same convention for other spaces such as $C^2(\Gamma)$ which is the space of twice continuously differentiable functions on Γ . As a consequence of the compactness, Fredholm's alternative implies that the operators

$$\left(\frac{1}{2}\mathcal{I} + \mathcal{K}\right) : C_*(\Gamma) \rightarrow C_{**}(\Gamma), \quad \text{and} \quad \left(\frac{1}{2}\mathcal{I} - \mathcal{K}'\right) : C(\Gamma) \rightarrow C(\Gamma)$$

are invertible. Here $C_*(\Gamma)$ is the space of all functions $u \in C(\Gamma)$ with

$$\int_{\Gamma} u(y) ds_y = 0 ,$$

and $C_{**}(\Gamma)$ is the space of all functions $u \in C(\Gamma)$ with

$$\int_{\Gamma} u(y) w_{eq}(y) ds_y = 0 ,$$

where $w_{eq} = \mathcal{V}^{-1}1$ is the natural weight, which has been used in analysis of the hyper-singular operator [58]. Further, compactness of \mathcal{K} and \mathcal{K}' implies that SBIE and HSBIE should be solved by inverting $\frac{1}{2}\mathcal{I} + \mathcal{K}$ and $\frac{1}{2}\mathcal{I} - \mathcal{K}'$, respectively.

For the pure Neumann BVP, the SBIE takes the form

$$\left(\frac{1}{2}\mathcal{I} + \mathcal{K} \right) u = \mathcal{V}g_N \quad \text{on } \Gamma. \quad (5)$$

Since $\mathcal{V} : C(\Gamma) \rightarrow C(\Gamma)$ and the boundary data g_N must satisfy the solvability condition

$$\int_{\Gamma} g_N(x) ds_x = 0 ,$$

it follows that $g_N \in C(\Gamma)$ implies $\mathcal{V}g_N \in C_{**}(\Gamma)$. Therefore, the invertibility of $(\frac{1}{2}\mathcal{I} + \mathcal{K})$ implies that (5) has a unique solution for $u \in C_*(\Gamma)$.

For the pure Dirichlet BVP, the HSBIE takes the form

$$\left(\frac{1}{2}\mathcal{I} - \mathcal{K}' \right) t = \mathcal{D}g_D \quad \text{on } \Gamma. \quad (6)$$

One can prove that $g_D \in C^2(\Gamma)$ implies $\mathcal{D}g_D \in C(\Gamma)$. Thus the invertibility of $(\frac{1}{2}\mathcal{I} - \mathcal{K}')$ implies that (6) has a unique solution for $t \in C(\Gamma)$.

Based on analysis of the pure BVPs, it is appropriate to require $g_D \in C^2(\Gamma_D)$ and $g_N \in C(\Gamma_N)$ for the mixed BVP. These restrictions, however, do not guarantee $u \in C^2(\Gamma)$ and $t \in C(\Gamma)$. To formulate the BIEs corresponding to the mixed BVP, we define extensions $\tilde{g}_D \in C^2(\Gamma)$ and $\tilde{g}_N \in C(\Gamma)$, and express the Cauchy data as

$$u = \tilde{u} + \tilde{g}_D \quad \text{and} \quad t = \tilde{t} + \tilde{g}_N. \quad (7)$$

By construction, $\tilde{u}|_{\Gamma_D} = 0$ and $\tilde{t}|_{\Gamma_N} = 0$. Now we can rewrite the SBIE and HSBIE as the equations for \tilde{u} and \tilde{t} :

$$\mathcal{V}\tilde{t} - \left(\frac{1}{2}\mathcal{I} + \mathcal{K} \right) \tilde{u} = \left(\frac{1}{2}\mathcal{I} + \mathcal{K} \right) \tilde{g}_D - \mathcal{V}\tilde{g}_N \quad \text{on } \Gamma, \quad (8)$$

and

$$\left(\frac{1}{2}\mathcal{I} - \mathcal{K}' \right) \tilde{t} - \mathcal{D}\tilde{u} = \mathcal{D}\tilde{g}_D - \left(\frac{1}{2}\mathcal{I} - \mathcal{K}' \right) \tilde{g}_N \quad \text{on } \Gamma. \quad (9)$$

Note that while \tilde{g}_D and \tilde{g}_N are not uniquely defined, the structure of (8) and (9) is such that u and t are uniquely defined as long as (8) and (9) are uniquely solvable for \tilde{u} and \tilde{t} . Since $\tilde{g}_D \in C^2(\Gamma)$ and $\tilde{g}_N \in C(\Gamma)$, the right-hand sides of both equations are in $C(\Gamma)$. However, this is insufficient for establishing unique solvability for (8) and (9), under the provisions $\tilde{u} \in C^2(\Gamma)$ and $\tilde{t} \in C(\Gamma)$.

Remark 2.1. It is straightforward to extend our analysis to the pure Robin BVP in which the boundary data are prescribed as

$$t + \kappa u = g_R \quad \text{on } \Gamma ,$$

where $\kappa \in L^\infty(\Gamma)$ and g_R is a prescribed function in $C(\Gamma)$. This problem is similar to the pure Neumann problem.

Remark 2.2. The regularity requirements on Γ , g_D and g_N can be slightly relaxed. The results of this section can be extended to continuously differentiable Γ , g_D with Lipschitz continuous derivatives, and $g_N \in L^\infty$.

Remark 2.3. While it appears that the condition $\tilde{g}_D \in C^2(\Gamma)$ is too restrictive, in practice g_D is often a constant. For example, in the context of heat conduction, Dirichlet boundary conditions represent a situation in which Ω is placed in a constant-temperature environment whose temperature is not affected by Ω . If it is the case, a constant g_D is simply extended to the entire boundary, so that \tilde{g}_D is constant.

3 Collocation discretization

Let us consider the mixed BVP. Approximations for \tilde{u} and \tilde{t} are constructed as

$$\tilde{u}_h(x) = \sum_{A=1}^{n^D} \tilde{u}[A] N_A^D(x), \quad \text{and} \quad \tilde{t}_h(x) = \sum_{A=1}^{n^N} \tilde{t}[A] N_A^N(x),$$

respectively, where $N_A^D(x)$ and $N_A^N(x)$ are the basis functions and \tilde{u} and \tilde{t} are column-vectors. Since $\tilde{u}(x) = 0$ for $x \in \Gamma_D$ and $\tilde{t}(x) = 0$ for $x \in \Gamma_N$, the basis functions are such that $N_A^D(x) = 0$ for $x \in \Gamma_D$ and $N_A^N(x) = 0$ for $x \in \Gamma_N$. Accordingly, we define collocation points x_A^D on Γ_N and x_A^N on Γ_D . This assignment of the superscripts may be somewhat confusing, but it simply reflects the fact that the basis functions $N_A^D(x)$ and $N_A^N(x)$ are supported on Γ_N and Γ_D , respectively.

Upon collocating (8) at x_A^D and (9) at x_A^N , one generates the system of linear algebraic equations for \tilde{u} and \tilde{t} :

$$V\tilde{t} - \left(\frac{1}{2}I_D + K\right)\tilde{u} = \underline{f}_S \quad (10)$$

and

$$\left(\frac{1}{2}I_N - K'\right)\tilde{t} - D\tilde{u} = \underline{f}_H. \quad (11)$$

Here the components of the system matrices are defined as

$$V[A, B] := \mathcal{V} N_B^N(x_A^D) = \int_{\Gamma_D} G(x_A^D, y) N_B^N(y) ds_y, \quad (12)$$

$$I_D[A, B] := N_B^D(x_A^D), \quad (13)$$

$$K[A, B] := \mathcal{K} N_B^D(x_A^D) = \int_{\Gamma_N} n(y) \cdot [\nabla_y G(x_A^D, y)] N_B^D(y) ds_y, \quad (14)$$

$$I_N[A, B] := N_B^N(x_A^N), \quad (15)$$

$$K'[A, B] := \mathcal{K}' N_B^N(x_A^N) = \int_{\Gamma_D} n(x_A^N) \cdot [\nabla_x G(x_A^N, y)] N_B^N(y) ds_y, \quad (16)$$

$$D[A, B] := \mathcal{D} N_B^D(x_A^N) = - \int_{\Gamma_N} n(x_A^N) \cdot \{ \nabla_x [n(y) \cdot \nabla_y G(x_A^N, y)] \} N_B^D(y) ds_y. \quad (17)$$

The right-hand-side vectors are defined as

$$\begin{aligned}\underline{f}_S[A] &:= \frac{1}{2}\tilde{g}_D(x_A^D) + \mathcal{K}\tilde{g}_D(x_A^D) - \mathcal{V}\tilde{g}_N(x_A^D), \\ \underline{f}_H[A] &:= \mathcal{D}\tilde{g}_D(x_A^N) - \frac{1}{2}\tilde{g}_N(x_A^N) + \mathcal{K}'\tilde{g}_N(x_A^N).\end{aligned}$$

For the pure Neumann BVP, all collocation points are x_A^D , and therefore it is sufficient to solve (10) by setting $\tilde{t}_h = 0$, $\tilde{g}_D = 0$, and $\tilde{g}_N = g_N$:

$$-\left(\frac{1}{2}I_D + K\right)\underline{\tilde{u}} = \underline{f}_S. \quad (18)$$

The compactness of \mathcal{K} can be used to show that (18) is uniquely solvable as long as

$$\int_{\Gamma} \tilde{u}_h(x) ds_x = 0. \quad (19)$$

Furthermore, under condition (19), \tilde{u}_h converges to the exact solution u of (5) at optimal rates.

For the pure Dirichlet BVP, all collocation points are x_A^N , and therefore it is sufficient to solve (11) by setting $\tilde{u}_h = 0$, $\tilde{g}_N = 0$, and $\tilde{g}_D = g_D$:

$$\left(\frac{1}{2}I_N - K'\right)\underline{\tilde{t}} = \underline{f}_H. \quad (20)$$

The compactness of \mathcal{K}' can be used to show that (20) is uniquely solvable and \tilde{t}_h converges to the exact solution t of (6) at optimal rates.

Remark 3.1. *It is straightforward to extend the collocation scheme to the pure Robin BVP following the prescription for the Neumann BVP. Also, for the pure Robin BVP, unique solvability and optimal convergence rates can be established in a way similar to the pure Neumann BVP.*

Remark 3.2. *In all cases, the system of governing algebraic equations is constructed so that one has to invert matrices associated with the operators $\frac{1}{2}\mathcal{I} + \mathcal{K}$ and $\frac{1}{2}\mathcal{I} - \mathcal{K}'$. This construction results in well-conditioned linear algebraic systems [2], and it is superior to alternative formulations; see Section 6 for numerical examples.*

4 Regularization of operators

In general, the SBIE and HSBIE involve integrals containing weakly-singular, singular, and hyper-singular kernels. In this section, we establish that for $\Gamma \in C^2$ and sufficiently smooth functions, as established in Section 2, all integrals can be evaluated as weakly singular ones. This property is essential as it allows one to develop numerical integration schemes with spectral accuracy [52].

The single-layer operator \mathcal{V} is naturally weakly singular for the continuous data; the same is true for \mathcal{K} and \mathcal{K}' (see Appendix). To regularize the hyper-singular operator \mathcal{D} we begin with approximating $u \in C^2(\Gamma)$ in the vicinity of x :

$$u(y) = u(x) + (\nabla_T u)(x) \cdot (y - x) + \mathcal{O}(|x - y|^2), \quad (21)$$

where $(\nabla_T u)(x)$ is the tangential gradient of u on Γ . With this approximation, the hyper-singular operator can be expressed as

$$\begin{aligned}\mathcal{D}u(x) &= - \int_{\Gamma} n(x) \cdot \nabla_x \{n(y) \cdot [\nabla_y G(x, y)]\} u(y) ds_y \\ &= - \int_{\Gamma} n(x) \cdot \nabla_x \{n(y) \cdot [\nabla_y G(x, y)]\} [u(y) - u(x) - (\nabla_T u)(x) \cdot (y - x)] ds_y \\ &\quad - u(x) \int_{\Gamma} n(x) \cdot \nabla_x \{n(y) \cdot [\nabla_y G(x, y)]\} ds_y - \int_{\Gamma} n(x) \cdot \nabla_x \{n(y) \cdot [\nabla_y G(x, y)]\} (\nabla_T u)(x) \cdot (y - x) ds_y.\end{aligned}\tag{22}$$

Since constant and linear functions are harmonic, the HSBIE implies that

$$\begin{aligned}- \int_{\Gamma} n(x) \cdot \nabla_x \{n(y) \cdot [\nabla_y G(x, y)]\} ds_y &= 0, \\ - \int_{\Gamma} n(x) \cdot \{ \nabla_x n(y) \cdot [\nabla_y G(x, y)] \} (\nabla_T u)(x) \cdot (y - x) ds_y &= - \int_{\Gamma} n(x) \cdot \nabla_x [G(x, y)] n(y) \cdot (\nabla_T u)(x) ds_y.\end{aligned}$$

Now the last line of (22) can be rewritten as

$$\begin{aligned}\mathcal{D}u(x) &= - \int_{\Gamma} n(x) \cdot \nabla_x \{n(y) \cdot [\nabla_y G(x, y)]\} [u(y) - u(x) - (\nabla_T u)(x) \cdot (y - x)] ds_y \\ &\quad - \int_{\Gamma} n(x) \cdot \nabla_x [G(x, y)] n(y) \cdot (\nabla_T u)(x) ds_y.\end{aligned}$$

In this equation, the first term on the right-hand side is weakly singular because of (21) and the second term is weakly singular because it is equal to $\mathcal{K}'[n(y) \cdot (\nabla_T u)(x)]$. Our development closely follows that in [36]. An important aspect of the regularization scheme is computing the tangential gradient. This issue will be addressed in Section 5 once IgA parametrizations have been introduced.

5 Isogeometric Analysis

5.1 CAD geometry

In IgA it is presumed that the surface Γ is described using a CAD tool. Invariably those descriptions rely on B-splines. A one-dimensional B-spline of degree p is a piecewise polynomial function of degree p . The smoothness between polynomials can be controlled locally and can be up to C^{p-1} . Thus, if desired, one can construct a B-spline of degree p , which is C^{p-1} globally. Multi-dimensional B-splines are constructed as tensor products of one-dimensional B-splines. T-splines are constructed as linear combinations of B-splines without the need for the tensor-product structure. This feature is very attractive, as it allows local refinement with hanging nodes, and therefore we use T-splines. For further details on T-splines we refer to [53, 54].

First, let us assume that Γ can be mapped on a rectangular parametric domain $\hat{\Gamma} \subset \mathbb{R}^2$. In CAD the map $\varphi : \hat{\Gamma} \rightarrow \Gamma$ is constructed in terms of a set of control points $P_A \in \mathbb{R}^3$, weights $w_A > 0$, and T-splines \hat{N}_A^T defined on $\hat{\Gamma}$:

$$x = \varphi(\xi_1, \xi_2) := \frac{\sum_A P_A w_A \hat{N}_A^T(\xi_1, \xi_2)}{\sum_B w_B \hat{N}_B^T(\xi_1, \xi_2)} \quad (\xi_1, \xi_2) \in \hat{\Gamma}.\tag{23}$$

This map has numerous advantages over the simpler map $\sum_A P_A \hat{N}_A^T(\xi_1, \xi_2)$. In particular, it can represent quadric surfaces exactly. Further, since T-splines \hat{N}_A^T are a superset of B-splines, the map (23) can be restricted to NURBS, which are currently an industrial standard. Note that in principle the map smoothness can be controlled by choosing appropriately smooth T-splines. However, in practice it is standard to set

$p = 3$ and use C^2 T-splines, so that $\varphi \in C^2(\hat{\Gamma})$. By adopting a global definition for the map $\psi := \varphi$, we conclude that Γ defined by φ is a C^2 -surface.

The map defined in (23) requires a rectangular $\hat{\Gamma}$ and therefore it is rather limited. For example, it cannot be used for constructing a cube. In the context of NURBS, this issue is usually addressed by allowing the parametric domain to consist of multiple rectangular patches. This creates a new host of problems associated with imposing continuity conditions across patches. This issue is naturally resolved with T-splines, as they allow for hanging nodes and smooth basis functions across patches. Nevertheless, even with T-splines, one has to address extraordinary points. By definition, those points are intersections of three or more than four patches. At extraordinary points, the parametrization map φ is only C^0 , and as a result $\Gamma \in \tilde{C}^2$. For details we refer to [54]. Another way of generalizing (23) is by allowing rectangles to be mapped on triangles by collapsing edges. This approach involves two ingredients: (i) in the parametric domain, all T-splines, supported on the edge to be collapsed, are constructed as C^0 functions across the edge, and (ii) control points corresponding to T-splines supported on the edge to be collapsed are assigned to the same position. Like the treatment of extraordinary points, this construction yields locally C^0 -parametrizations. Thus generalized maps, involving multiple rectangular patches, give rise to $\Gamma \in \tilde{C}^2$.

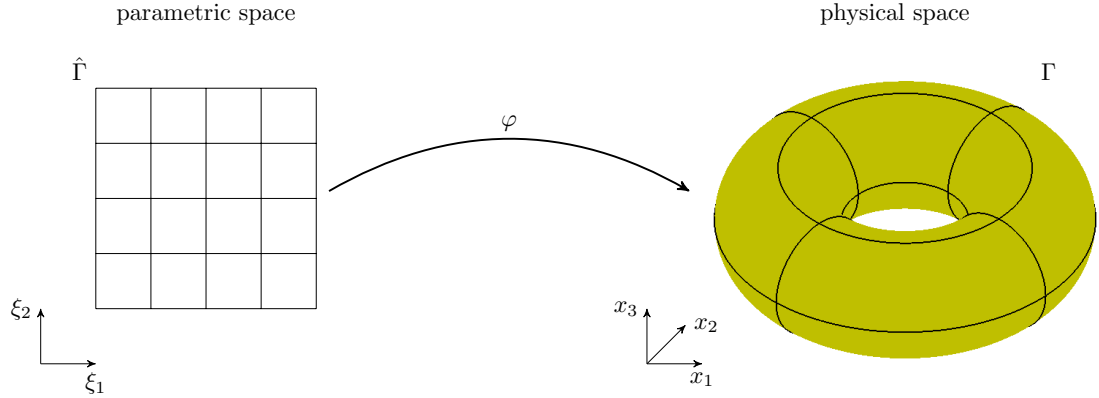


Figure 1: Parametric and physical spaces for a torus.

5.2 Basis functions

Let us suppose that control points P_A , weights w_A , and T-splines \hat{N}_A^T , prescribing Γ via (23) are given. Then in the parametric domain the basis functions are constructed using the partition of unity

$$\hat{N}_A(\xi_1, \xi_2) := \frac{w_A \hat{N}_A^T(\xi_1, \xi_2)}{\sum_{B=1}^n w_B \hat{N}_B^T(\xi_1, \xi_2)}. \quad (24)$$

The basis functions N_A in the physical domain Γ are constructed via the standard map

$$N_A := \hat{N}_A \circ \varphi^{-1}. \quad (25)$$

This construction includes extraordinary points but not collapsed edges. For the latter cases, the basis functions $\hat{N}_{A'}$ supported on a collapsed edge are replaced by a single basis function

$$\hat{N} = \sum_{A'} \hat{N}_{A'}.$$

After that, the corresponding basis function N is constructed via (25). Note that in our work, both extraordinary points and collapsed edges give rise to basis functions which are locally C^2 but globally continuous. For extraordinary points, one could use a constrained optimization framework that gives rise to C^1 -basis functions; for details see [54].

For solving BIEs, one also needs discontinuous basis functions for approximating t , which can be discontinuous and even singular even if $\Gamma \in C^2$ and prescribed Cauchy data are smooth. It is straightforward to define discontinuous T-splines $\hat{N}_A^{T,\text{disc}}$. However, CAD parametrizations involve the weights for continuous T-splines only. While, in principle, one can compute the weights for discontinuous T-splines, and then use (24), we adopt a simpler construction involving unweighted scaled basis functions:

$$\hat{N}_A(\xi_1, \xi_2) := \frac{\hat{N}_A^{T,\text{disc}}(\xi_1, \xi_2)}{\sum_{B=1}^n w_B \hat{N}_B^T(\xi_1, \xi_2)}. \quad (26)$$

The scaling by $\left[\sum_{B=1}^n w_B \hat{N}_B^T(\xi_1, \xi_2)\right]^{-1}$ is motivated by numerical examples rather than theory. The construction in (26) is not a partition of unity, but this property is not required for analysis of BIEs.

5.3 Collocation points

The Greville abscissa of a B-spline is a point in the parametric domain $\hat{\Gamma}$ whose coordinates are defined as the average of the coordinates of the knots. These points often correspond to the maximum value of the B-spline. It has been shown that they are ideally suited for interpolation and that they can be naturally extended to T-splines. Further, Greville abscissae have been widely used as collocation points for the basis functions (25) in various numerical methods [6, 4, 50], including those for BIEs [38, 54, 56, 57]. However, it has been recognized [54] that for discontinuous T-splines Greville's abscissae may coincide, and therefore one needs to modify the construction. This issue has been addressed by introducing "2-ring" collocation points [54] for discontinuous cubic T-splines.

In this work, we generalize the definition of the "2-ring" collocation points to T-splines of degree p . To this end, let us consider a one-dimensional B-spline $B(\xi)$ of degree p with $a \leq \xi \leq b$. If $B(\xi) \in C([a, b])$, then the "2-ring" collocation point is simply Greville abscissa. If $B(\xi)$ is discontinuous at $\xi = a$ then the "2-ring" collocation point is

$$\xi_{2\text{-ring}} := a + \frac{b-a}{p+2};$$

if the discontinuity is at $\xi = b$, then

$$\xi_{2\text{-ring}} := b + \frac{a-b}{p+2}.$$

To construct the collocation point for a two-dimensional discontinuous T-spline, we can exploit that locally (rather than globally) T-splines are tensor products of one-dimensional B-splines. Therefore once a two-dimensional discontinuous T-spline is represented by $T_{ij}(\xi_1, \xi_2) = B_i(\xi_1)B_j(\xi_2)$, one can find the coordinates of the "2-ring" collocation point by treating $B_i(\xi_1)$ and $B_j(\xi_2)$ separately.

5.4 Numerical Integration

It has been established in Section 4 that, upon collocation, all operators can be evaluated as weakly-singular integrals on C^2 -surfaces. In this section, we focus on numerical integration schemes applicable to the operators on \tilde{C}^2 -surfaces. First, let us establish that all operators can be evaluated as weakly-singular integrals on \tilde{C}^2 -surfaces, as long as approximations are allowed to include discontinuous basis functions. This provision is essential as it allows one to move the collocation points away from surface irregularities, associated with either CAD parametrizations of smooth surfaces (extraordinary points and collapsed edges) or non-smooth surfaces.

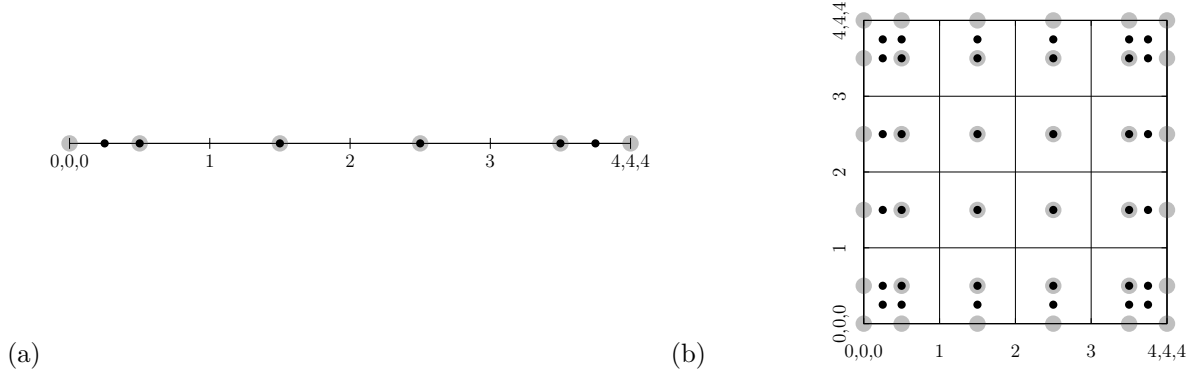


Figure 2: Greville abscissae (large grey circles) and “2-ring” Greville abscissae (small black circles) for a single patch in (a) 1-D and (b) 2-D. Note that the abscissae coincide except for the patch boundaries.

For discontinuous basis functions the collocation points are restricted to the smooth part of Γ . Then among the operators defined in (12), \mathcal{K}' and \mathcal{D} can be evaluated using weakly-singular integrals because they operate on functions that are smooth in neighborhoods of the collocation points. Then local Taylor expansions can be exploited for regularization, similar to the way it is done in Section 4. Further, the operator \mathcal{V} is naturally weakly singular on \tilde{C}^2 -surfaces. To establish weak singularity of $(\sigma\mathcal{I} + \mathcal{K})u$, let us substitute $u(x) = 1$ in the SBIE to obtain

$$(\sigma\mathcal{I} + \mathcal{K})1 = 0$$

and the regularization

$$(\sigma\mathcal{I} + \mathcal{K})u(x) = \int_{\Gamma} n(y) \nabla_y G(x, y) u(y) [u(y) - u(x)] ds_y .$$

Note that we replaced $1/2$ with σ to reflect the fact that Γ is not smooth near certain x . This regularization is not sufficient for making the integral weakly singular for $u \in C(\Gamma)$. On the other hand if u is Lipschitz continuous, so that

$$|u(y) - u(x)| < C |y - x| ,$$

then the integral becomes weakly singular. This additional restriction on $u(x)$ does not pose problems within the context of IgA.

As usual, in IgA all integrals are evaluated in the parametric domain $\hat{\Gamma}$. Thus numerical integration schemes have to be developed, so that they properly take into account the geometric parametrization. In particular, the weak singularity, established in the physical domain Γ , should be preserved for integrals defined over the parametric domain $\hat{\Gamma}$. Further, since $\hat{\Gamma}$ is partitioned into Bézier elements, defined such that within each element the supported T-splines are C^∞ , locally, the map φ and the basis functions are also C^∞ . This is sufficient for developing numerical integration schemes with spectral accuracy [52]. If the integrations were carried out in the physical domain, then it would be natural to use curvilinear coordinates attached to the surface. Accordingly, if one uses parametric coordinates, one needs to rely on differential geometry. Alternatively, one can avoid explicit use of curvilinear coordinates by constructing a transformation based on the singular-value decomposition theorem [19]. This transformation is constructed as follows:

1. At a given collocation point, compute the vectors τ^1 and τ^2 as

$$\tau^1 = \frac{\partial \varphi(\eta_1, \eta_2)}{\partial \eta_1} \quad \text{and} \quad \tau^2 = \frac{\partial \varphi(\eta_1, \eta_2)}{\partial \eta_2} ,$$

where (η_1, η_2) are the coordinates of the collocation point in $\hat{\Gamma}$.

2. Form a Jacobian matrix

$$J = \begin{pmatrix} \tau_1^1 & \tau_1^2 \\ \tau_2^1 & \tau_2^2 \\ \tau_3^1 & \tau_3^2 \end{pmatrix},$$

where the subscripts refer to the Cartesian components in a global coordinate system, in which the control points are prescribed.

3. Compute the reduced singular-value decomposition

$$J = U\Sigma V^*,$$

so that U is a 3×2 matrix and Σ is a 2×2 diagonal matrix with no zeros on the diagonal.

4. Define the reparametrization $\bar{\varphi}(\bar{\xi}_1, \bar{\xi}_2)$ of $\varphi(\xi_1, \xi_2)$ via

$$\varphi(\xi_1, \xi_2) = \bar{\varphi}(\bar{\xi}_1, \bar{\xi}_2) = \varphi(V\Sigma^{-1}\bar{\xi}),$$

where $\bar{\xi} = (\bar{\xi}_1, \bar{\xi}_2)^T$.

5. Compute the *orthonormal* vectors $\bar{\tau}^1$ and $\bar{\tau}^2$ as

$$\bar{\tau}^1 = \frac{\partial \bar{\varphi}(\bar{\xi}_1, \bar{\xi}_2)}{\partial \bar{\xi}_1} \quad \text{and} \quad \bar{\tau}^2 = \frac{\partial \bar{\varphi}(\bar{\xi}_1, \bar{\xi}_2)}{\partial \bar{\xi}_2},$$

where $(\bar{\xi}_1, \bar{\xi}_2)$ are the transformed parametric coordinates of the collocation point.

This reparametrization scheme, leading to orthonormal basis vectors, gives rise to optimal numerical integration schemes for weakly-singular integrals [52], [19]. Further, based on numerical results presented in Section 6, it appears that the reparametrization scheme is critical for numerical integration for CAD parametrizations involving collapsed edges.

Numerical integration in the parametric domain is carried out Bézier-element-wise. If the collocation point is inside the element, then we apply the reparametrization scheme $(\xi_1, \xi_2) \rightarrow (\bar{\xi}_1, \bar{\xi}_2)$, which transforms a rectangular element into a parallelogram, on which one can implement a standard singular integration scheme using a polar coordinate transformation [52]. If the collocation point is outside the element, then the integrand is regular, and one can use Gaussian quadratures, provided that the collocation point is not too close to the element. Typically, Gaussian quadratures work well for points located at a distance $d > 3h$, where h is an element size, and both dimensions are defined in the physical space Γ . If $d < 3h$ one can carry out recursive element subdivision, which reduces h until $d > 3h$. Thus, in effect, Gaussian quadratures are applied whenever the point is outside of the element, but for cases when $d < 3h$ one needs to combine Gaussian quadratures with recursive element subdivision.

6 Numerical Examples

6.1 Overview

In this section, we present numerical examples emphasizing various important mathematical and computational aspects of IgA of BIEs. All examples involve three shapes: a torus, a sphere, and a cube. The torus is a C^∞ -surface which allows a C^2 -parametrization; actually one can show that the torus parametrization is C^∞ but this additional smoothness is not exploited. The sphere is a C^∞ -surface with a \tilde{C}^2 -parametrization, because it involves collapsed edges at the poles. The cube is a \tilde{C}^2 -surface with a \tilde{C}^2 -parametrization. All shapes were constructed using standard parametrizations based on 16 (torus), 8 (sphere), and 6 (cube) NURBS patches. For each shape, the patches were used to generate five meshes via uniform refinement in the parametric domain, so that at each level of refinement, each element was divided into four. Figure

4 shows the two coarsest meshes for each shape. Continuous basis functions of degree p were constructed so that, upon refinement, they remained C^{p-1} locally and continuous over patch boundaries. In contrast to continuous basis functions, their discontinuous counterparts were C^{p-1} locally and discontinuous over patch boundaries. Unless otherwise noted, all regular approximations involved $p = 2$, and degree elevated approximations involved $p = 3$. The number of integration points in numerical integration schemes involving the polar coordinate transformation was dependent on the refinement level. At the coarse level, we used 5 points in the radial direction and 10 points in the angular direction. With each refinement, the number of points in the radial direction stayed the same, while the number of points in the angular direction was increased by three. For regular integrals, we used the 5×5 Gaussian quadrature rule on each subelement. These rules were established empirically and no attempts were made to optimize them.

The majority of numerical examples involved manufactured exact solutions in the form

$$u(x) = \frac{1}{|x - x_0|}. \quad (27)$$

For each shape the source point x_0 was chosen far away from the shape center (Fig. 3), so that $u(x)$ was an analytic function which did not involve near-singular behavior. These manufactured solutions were chosen in order to demonstrate the necessity of numerical schemes even for problems with smooth solutions. The function $u(x)$ was used to construct the boundary data g_D and/or g_N for various BVPs. After that, appropriate BIEs were solved numerically to reconstruct the full Cauchy data.

The quality of numerical solutions was measured using the $L^2(\Gamma)$ -error for the Cauchy data. To evaluate the order of convergence, we defined the mesh size h as the square root of the area of the largest Bézier element in the physical space. The estimated order of convergence (eoc) for each refinement was computed as

$$eoc = \frac{\log\left(\frac{e_f}{e_c}\right)}{\log\left(\frac{h_f}{h_c}\right)},$$

where the subscripts f and c refer to the fine and coarse meshes, respectively. For $p = 2$ the optimal order of convergence for the $L^2(\Gamma)$ -error for the Cauchy data is equal to $p + 1 = 3$.

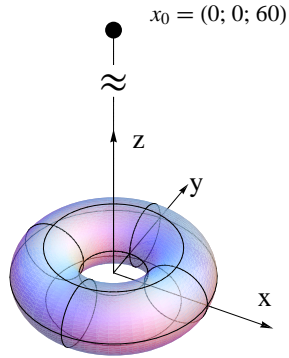
Unless stated otherwise, all arising algebraic problems were solved using a preconditioned GMRES method [47] with a tolerance of 10^{-12} . Each preconditioner was constructed as the inverse of the interpolation matrix corresponding to the basis functions. As a result, we were able to reveal the spectral properties of the collocated operators and significantly reduce the iteration count.

In the remainder of this section, we present six case studies. Each study demonstrates the importance of a particular aspect. Those studies focus on (i) the recursive subdivision scheme for near-singular integration (Section 6.2), (ii) local surface reparametrization (Section 6.3), (iii) exponential convergence of the adopted integration scheme (Section 6.4), (iv) spectral properties of the collocated operators (Section 6.5), (v) discontinuous basis functions (Section 6.6), and (vi) approximations for mixed BVPs (Section 6.7).

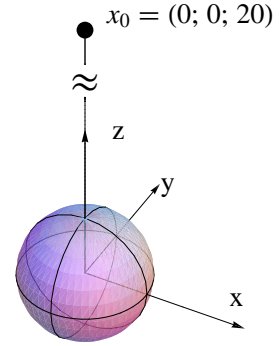
6.2 Recursive subdivision for near-singular integration

The objective of this section is to demonstrate that the recursive subdivision scheme (Section 5.4) for evaluating near-singular integrals is essential. To this end, we considered the manufactured pure Neumann BVP on the torus and established that the optimal order of convergence and accurate results can be attained only if the subdivision scheme was employed. The approximate solutions to this problem were obtained by solving (18) and (19), using continuous basis functions.

(a)



(b)



(c)

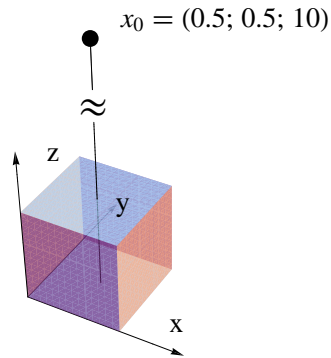
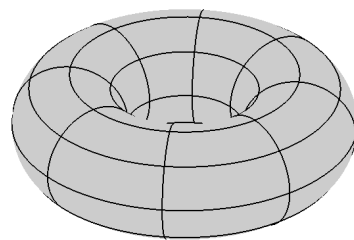
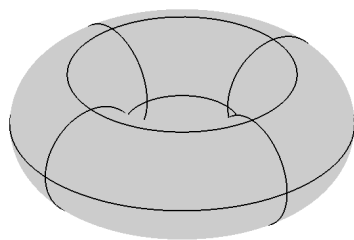
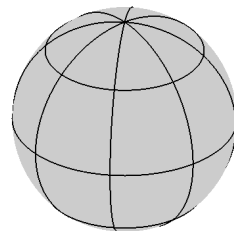
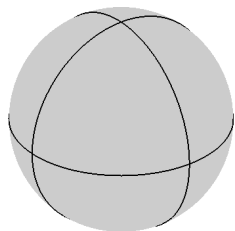


Figure 3: Three representative shapes: (a) torus (inner radius $r = 1$ and outer radius $R = 3$), (b) sphere (radius $r = 1$), and (c) cube (edge length $a = 1$). The source points for the manufactured solutions: $x_0 = (0, 0, 60)$ for the torus, $x_0 = (0, 0, 20)$ for the sphere, and $x_0 = (1/2, 1/2, 10)$ for the cube.

(a)



(b)



(c)

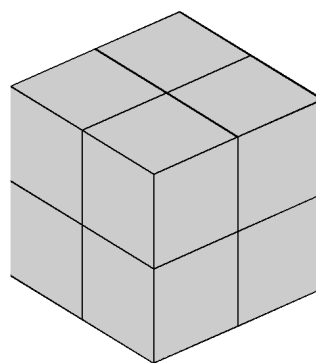
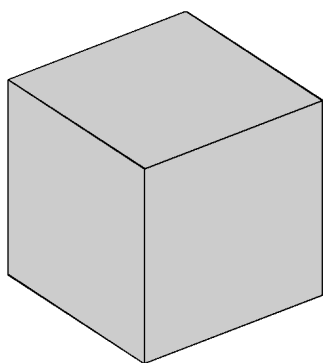
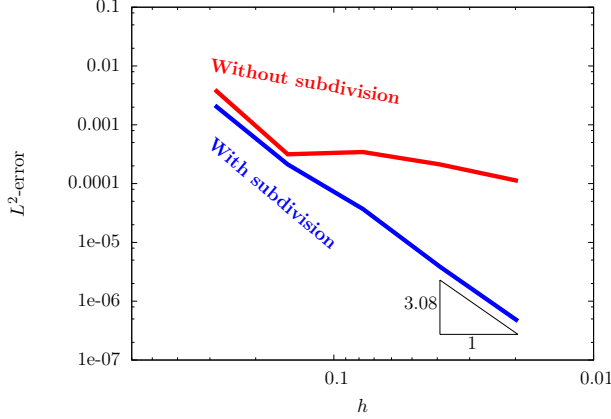


Figure 4: Meshes for the first two refinement levels for the (a) torus, (b) sphere, and (c) cube.

Figure 5 presents the $L^2(\Gamma)$ -error of \tilde{u}_h for two numerical integration schemes, with and without recursive subdivision. It is clear that recursive subdivision is necessary for attaining the optimal order of convergence. Furthermore, recursive subdivision significantly reduced the magnitude of the errors. The numerical example is representative of the other shapes and boundary conditions.



h	With subdivision		Without subdivision	
	L^2 -error	eoc	L^2 -error	eoc
2.87E-01	2.14E-03		3.95E-03	
1.51E-01	2.12E-04	3.58	3.15E-04	3.91
7.73E-02	3.71E-05	2.62	3.44E-04	-0.13
3.90E-02	3.87E-06	3.31	2.12E-04	0.71
1.96E-02	4.60E-07	3.08	1.11E-04	0.93

Figure 5: $L^2(\Gamma)$ -errors for two near-singular integration schemes: with and without subdivision.

6.3 Surface reparametrization scheme

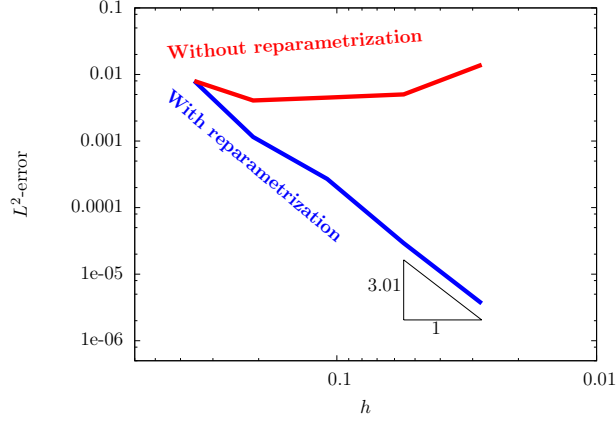
The objective of this section is to demonstrate the importance of the surface reparametrization scheme (Section 4) for evaluating singular integrals, particularly when collapsed edges are involved. To this end, we considered the manufactured pure Dirichlet BVP on the sphere. The approximate solutions to this problem were first obtained by using the SBIE and discontinuous basis functions. The corresponding linear algebraic problem is

$$V\tilde{t} = \underline{f}_S. \quad (28)$$

Note that the SBIE requires one to invert the matrix corresponding to the single-layer operator, which is not optimal, as far as the spectral properties are concerned. Nevertheless, it allows us to demonstrate that the surface reparametrization scheme is necessary even for a naturally weakly-singular operator.

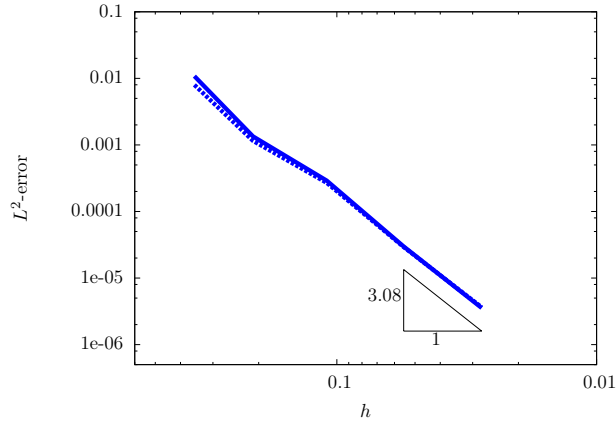
Figure 6 presents the $L^2(\Gamma)$ -error for the solutions of (28), using two numerical integration schemes, with and without the reparametrization. It is clear that the reparametrization is necessary for attaining the optimal order of convergence and small errors. This example is representative of other CAD parametrizations involving collapsed edges.

Alternatively, one can solve the manufactured problem using the HSBIE (20) and the discontinuous basis functions. In this case, similar to equation (28), the reparametrization scheme is necessary for accurate integration at collocation points near collapsed edges. Further the reparametrization scheme is natural for computing the tangent gradient required for regularizing the hyper-singular operator. Figure 7 presents the $L^2(\Gamma)$ -error of \tilde{t}_h on the sphere using SBIE and HSBIE; results for the SBIE are identical to those presented in Figure 6. It is clear that the two approaches yield similar results, and therefore both are acceptable. Thus we can conclude that the surface reparametrization scheme is necessary, and it is capable of delivering optimal and accurate numerical solutions even if the hyper-singular operator is involved.



h	With reparametrization		Without reparametrization	
	L^2 -error	eoc	L^2 -error	eoc
3.54E-01	7.99E-03		7.99E-03	
2.10E-01	1.15E-03	3.73	4.07E-03	1.30
1.09E-01	2.70E-04	2.22	4.49E-03	-0.15
5.53E-02	2.92E-05	3.26	5.01E-03	-0.16
2.77E-02	3.64E-06	3.01	1.40E-02	-1.48

Figure 6: The manufactured pure Dirichlet BVP for the sphere: $L^2(\Gamma)$ -errors for two singular integration schemes, with and without reparametrization.



h	SBIE		HSBIE	
	L^2 -error	eoc	L^2 -error	eoc
3.54E-01	7.99E-03		1.08E-02	
2.10E-01	1.15E-03	3.73	1.34E-03	4.01
1.09E-01	2.70E-04	2.22	2.91E-04	2.34
5.53E-02	2.92E-05	3.26	2.98E-05	3.34
2.77E-02	3.64E-06	3.01	3.55E-06	3.08

Figure 7: The manufactured pure Dirichlet BVP for the sphere: $L^2(\Gamma)$ -errors for two approaches, one based on the SBIE (dashed line) and the other based on the HSBIE (solid line).

6.4 Exponential convergence of the integration scheme

The objective of this section is to demonstrate that the adopted numerical integration scheme is exponentially convergent with respect to the number of integration points. The demonstration involves all three shapes. Thus the integration scheme was tested on problems involving non-smooth surfaces and parametrizations. For each shape, the test problem was a pure Neumann BVP with the exact solution

$$u(x) = x_1 + x_2 + x_3, \quad x \in \Omega.$$

For this choice, one can prove that the approximation error is exactly equal to zero for every shape, and therefore the chosen test problems are ideal for assessing numerical integration errors.

Figure 8 presents the $L^2(\Gamma)$ -error of the solution u_h . The results were obtained by using the coarsest meshes, while the number of integration points in each direction was increased. The results confirm an exponential convergence for every shape. Note that we were able to reach the machine precision for the sphere and the cube, while for the torus the error stagnated near 10^{-10} due to round-off errors in the adopted numerical integration scheme. If desired, this issue can be resolved by using a more sophisticated singular integration scheme proposed in [19].

6.5 Spectral properties of integral operators

It is well-known that, upon discretization, the operators $\frac{1}{2}\mathcal{I} + K$ and $\frac{1}{2}\mathcal{I} - K'$ give rise to well-conditioned matrices. The objective of this section is to demonstrate that one should choose the governing BIEs so that one takes advantage of this property. Accordingly, for pure Neumann BVPs, the SBIE is a natural choice. In contrast, for pure Dirichlet BVPs, one should choose the HSBIE. This choice would be problematic for conventional collocation BEMs but it is legitimate for IgA. This point will be supported by numerical examples presented in Section 6.5.1. Further, we show that for mixed boundary-value problems one should choose the SBIE on Γ_N and the HSBIE on Γ_D . Numerical examples presented in Section 6.5.2 show that, as far as spectral properties and iteration counts are concerned, this choice is superior than uniform use of SBIE. Numerical examples involved the manufactured solutions for all three shapes and results are presented for both iteration counts and condition numbers.

6.5.1 Dirichlet problems

In principle, a pure Dirichlet BVP can be solved using either the SBIE or HSBIE. The corresponding linear algebraic problems are

$$V\tilde{\underline{t}} = \underline{f}_S$$

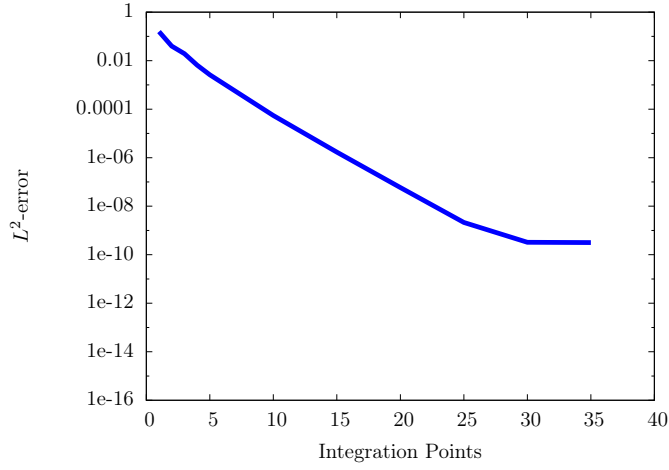
and

$$\left(\frac{1}{2}I_N - K'\right)\tilde{\underline{t}} = \underline{f}_H.$$

Thus the SBIE-based approach requires one to invert V , whereas the HSBIE-based approach requires one to invert $\frac{1}{2}I_N - K'$.

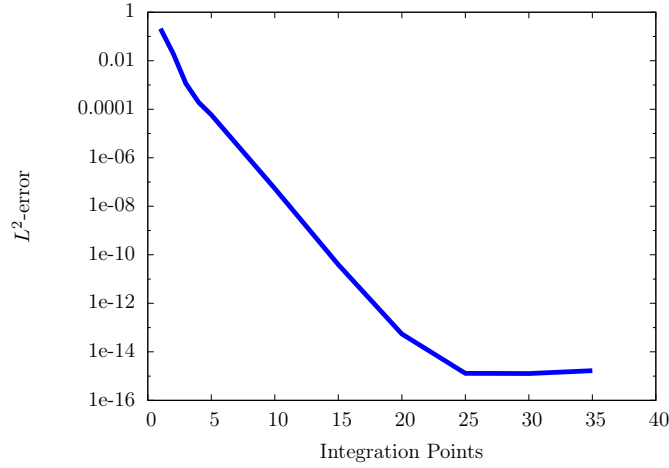
Figure 9 presents the iteration counts and spectral condition numbers κ as functions of h for the three shapes. It is clear that the HSBIE is a better choice than the SBIE both in terms of the iteration counts and spectral properties. For the torus and sphere, the iteration counts and spectral properties for the HSBIE are independent of the mesh size. This is in agreement with theoretical results based on compactness of K' . In this regard, let us observe that upon discretization the torus remains a C^2 -surface, whereas the sphere becomes a \tilde{C}^2 -surface. Thus the numerical results for the torus are fully expected, while the results for the sphere need additional theoretical considerations. For the cube, both the iteration count and the spectral condition number show a logarithmic dependence on h . For the cube, the mathematical foundations are not well-established because K' is not compact. For the SBIE, the iteration count should grow as $1/\sqrt{h}$ whereas κ should grow as $1/h$. Surprisingly, these scalings hold only for the cube. It is unclear to us why the results for the torus are better than expected and for the sphere worse than expected.

(a)



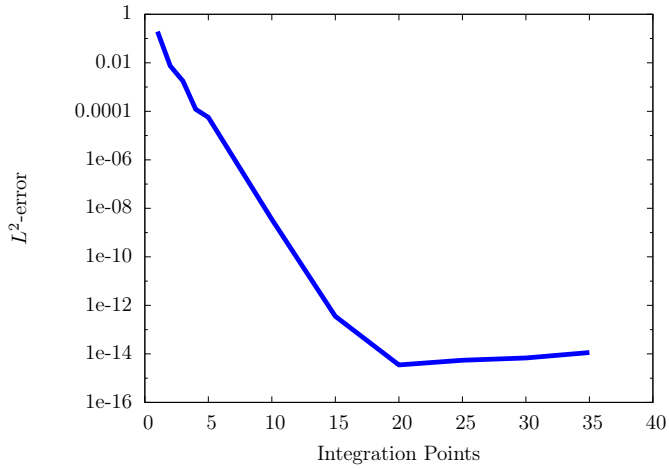
Int. Pts.	L^2 -error
1	1.58E-01
2	3.99E-02
3	1.93E-02
4	6.53E-03
5	2.62E-03
10	5.49E-05
15	1.70E-06
20	5.87E-08
25	2.14E-09
30	3.26E-10
35	3.16E-10

(b)



Int. Pts.	L^2 -error
1	2.10E-01
2	2.00E-02
3	1.14E-03
4	1.94E-04
5	5.92E-05
10	5.39E-08
15	3.94E-11
20	5.46E-14
25	1.30E-15
30	1.28E-15
35	1.67E-15

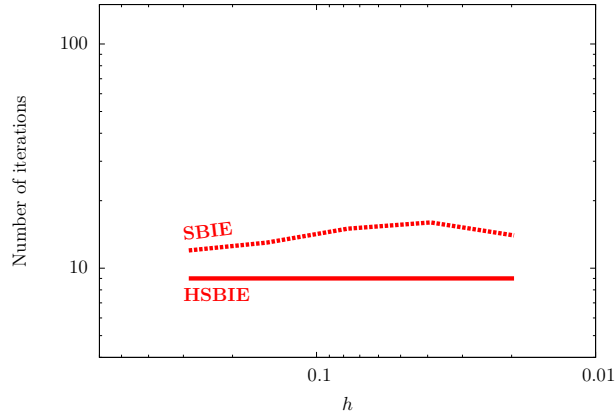
(c)



Int. Pts.	L^2 -error
1	1.94E-01
2	7.50E-03
3	1.75E-03
4	1.21E-04
5	5.66E-05
10	3.51E-09
15	3.55E-13
20	3.50E-15
25	5.44E-15
30	6.80E-15
35	1.14E-14

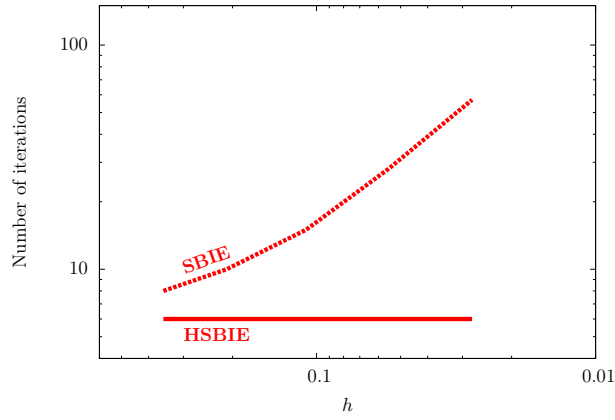
Figure 8: Numerical integration $L^2(\Gamma)$ -errors for the (a) torus (b) sphere, and (c) cube.

(a)



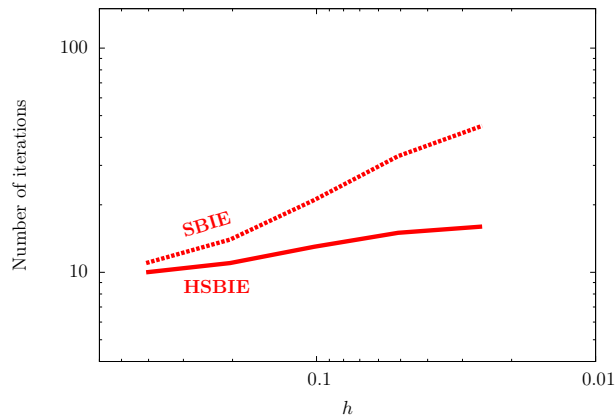
h	SBIE		HSBIE	
	Number of iterations	κ	Number of iterations	κ
2.87E-01	12	33.44	9	3.22
1.51E-01	13	68.86	9	3.27
7.73E-02	15	145.92	9	3.29
3.90E-02	16	276.92	9	3.12
1.96E-02	14	523.13	9	2.98

(b)



h	SBIE		HSBIE	
	Number of iterations	κ	Number of iterations	κ
3.54E-01	8	45.54	6	2.03
2.10E-01	10	154.29	6	2.23
1.09E-01	15	637.30	6	2.37
5.53E-02	28	2447.50	6	2.27
2.77E-02	57	9327.50	6	2.18

(c)



h	SBIE		HSBIE	
	Number of iterations	κ	Number of iterations	κ
4.08E-01	11	16.27	10	3.17
2.04E-01	14	25.49	11	3.39
1.02E-01	21	50.36	13	4.02
5.10E-02	33	97.01	15	4.36
2.55E-02	45	187.97	16	4.61

Figure 9: Iteration counts of the preconditioned GMRES method and condition numbers κ for the (a) torus (b) sphere, and (c) cube .

6.5.2 Mixed boundary-value problem

In this section, we present numerical examples suggesting that one should choose the SBIE on Γ_N and the HSBIE on Γ_D , as opposed to using the SBIE on the entire Γ . For our purposes, we choose boundary conditions as shown in Figure 10. For the torus and sphere, the Dirichlet (Neumann) boundary conditions are prescribed on the upper (lower) halves. For the cube, the Neumann boundary conditions are prescribed on the top and bottom faces, and the Dirichlet boundary conditions on the other faces. Similar to pure

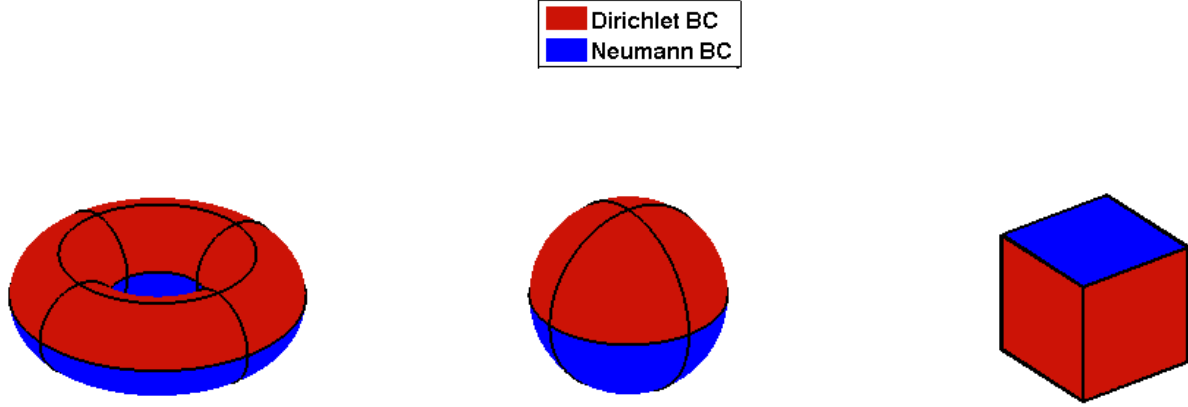


Figure 10: Mixed boundary conditions for the torus, sphere, and cube.

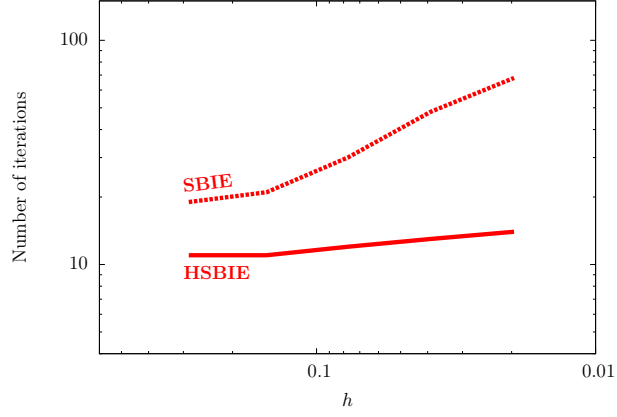
Dirichlet BVPs, mixed BVPs can be solved with our without the HSBIE. We refer to the former method as SBIE/HSBIE and to the latter one SBIE/SBIE. In the SBIE/HSBIE, the natural domain for the HSBIE is Γ_D , as in Dirichlet BVPs, while the SBIE is natural for Γ_N . In the SBIE/SBIE, the SBIE must be applied in its unnatural domain Γ_D . In terms of linear algebra, SBIE/HSBIE allows one to avoid inverting matrices with unfavorable spectral properties.

Figure 11 presents the iteration counts for the mixed BVPs for the three shapes. It is clear that (i) the SBIE/HSBIE is superior to SBIE/SBIE, and (ii) the iteration counts grow with mesh-refinement for all three problems; for the SBIE/HSBIE scheme, the iteration counts grow logarithmically with h^{-1} . We do not present comparisons for the spectral properties because such comparisons strongly depend on the definition of spectral properties. That is, the spectral properties for the entire matrices are different from those obtained using Schur complements; in contrast, the use of Schur complements has minimal effects on iteration counts.

6.6 Discontinuous basis functions

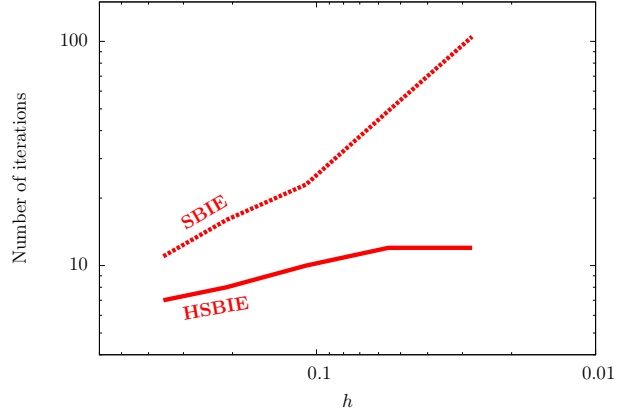
The objective of this section is to demonstrate that discontinuous basis functions are critical for approximating t when it is discontinuous. Those problems include not only non-smooth domains like a cube, but also mixed BVPs defined on smooth domains; in the latter case, t may be discontinuous at the interface between Γ_D and Γ_N . For demonstration purposes, we solved the manufactured pure Dirichlet BVP on the cube. In this problem, t is discontinuous at the edges and vertices because of the discontinuous normal. Further, the normal discontinuity does not allow us to collocate the operators $\frac{1}{2}\mathcal{I} - \mathcal{K}'$ and \mathcal{D} at the edges and vertices. This creates two options: (i) one can use the SBIE with either continuous or discontinuous basis functions, or (ii) one can use either the SBIE or HSBIE with discontinuous basis functions because they require collocation points off the edges and vertices. We pursue the first option as it allows us to compare continuous versus discontinuous basis functions.

(a)



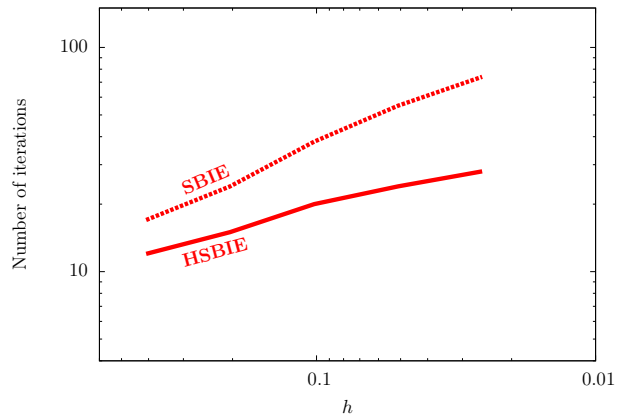
h	SBIE/SBIE	SBIE/HSBIE
2.87E-01	19	11
1.51E-01	21	11
7.73E-02	30	12
3.90E-02	48	13
1.96E-02	68	14

(b)



h	SBIE/SBIE	SBIE/HSBIE
3.54E-01	11	7
2.10E-01	16	8
1.09E-01	23	10
5.53E-02	49	12
2.77E-02	105	12

(c)



h	SBIE/SBIE	SBIE/HSBIE
4.08E-01	17	12
2.04E-01	24	15
1.02E-01	38	20
5.10E-02	55	24
2.55E-02	74	28

Figure 11: Iteration counts of the preconditioned GMRES method for the (a) torus, (b) sphere, and (c) cube.

Figure 12 presents the $L^2(\Gamma)$ -error of \tilde{t}_h for two approximations, one involves only continuous basis functions and the other only discontinuous ones. It is clear that for the continuous basis functions \tilde{t}_h converges very slowly. In contrast, for the discontinuous basis functions, \tilde{t}_h converges at the optimal rate and delivers very accurate solutions.

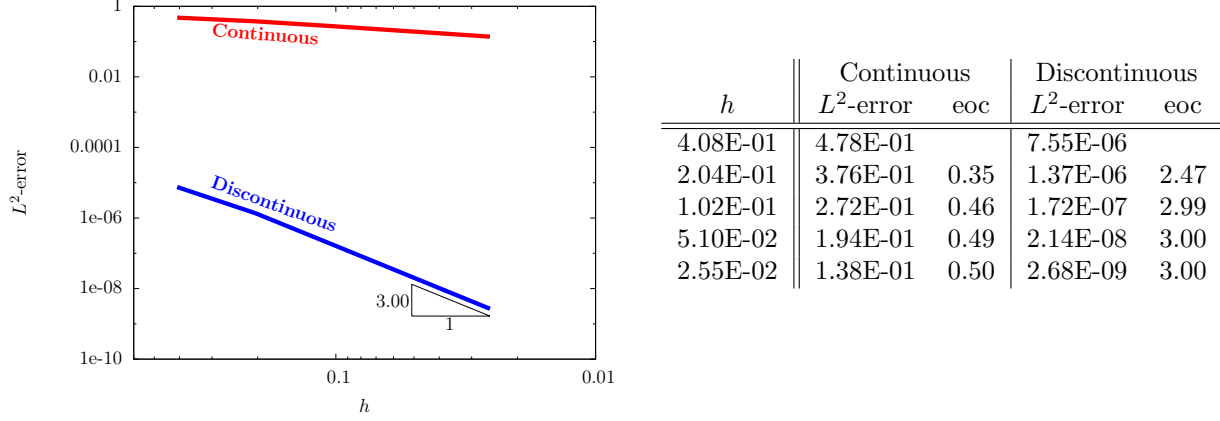


Figure 12: $L^2(\Gamma)$ -errors for two approximations, with and without the discontinuous basis functions.

6.7 Approximations for mixed boundary-value problems

In approximation theory for BIEs, it is well established that for mixed boundary-value problems one should use different approximations for the Cauchy data u and t . In particular, to attain the optimal convergence rate for the Cauchy data, approximations for u should be one degree higher than those for t [58]. In this section, we present numerical results supporting this statement. Further, we present results suggesting that approximations of the same degree are capable of delivering the optimal convergence rate for the torus and sphere.

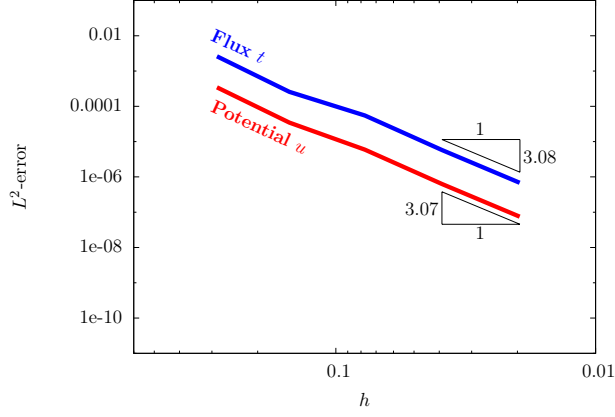
For demonstration purposes, we considered the same mixed BVPs as in Section 6.5. These problems were solved using the SBIE/HSBIE scheme, discontinuous basis functions for approximating t , and continuous regular ($p = 2$) and degree elevated ($p = 3$) basis functions for approximating u . Figure 13 presents the $L^2(\Gamma)$ -errors obtained using regular basis functions for u . It is clear that the $L^2(\Gamma)$ -error for u converges optimally for all three cases. In contrast, the rate of convergence for t is optimal for the torus and sphere, but not for the cube. Perhaps the results for the torus and sphere are more surprising than those for the cube, as we expected suboptimal convergence rates for t for all three cases.

Figure 14 presents the $L^2(\Gamma)$ -errors obtained using degree elevated basis functions for u . It is clear that in all three cases the $L^2(\Gamma)$ -errors for both u and t exhibit optimal convergence rates. Note that for the cube the errors corresponding to the degree elevated basis functions are significantly smaller than those corresponding to the regular basis functions. For the torus and sphere, the errors in u corresponding to the degree elevated basis functions are also significantly smaller than those corresponding to the regular basis functions, which is not surprising simply because we used higher-order approximations. In contrast, for the torus and sphere, the degree elevated approximation for u had a minor impact on the errors for t .

7 Summary

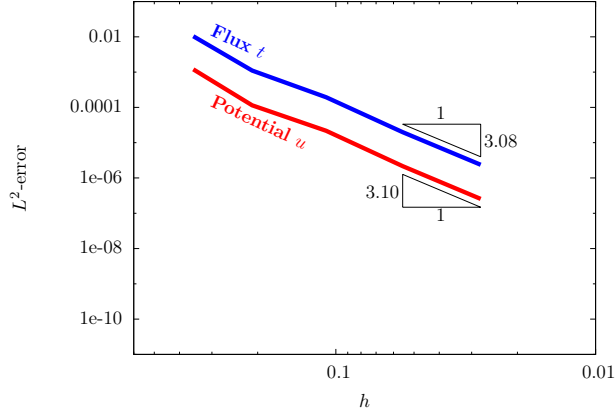
In this paper, we adopted IgA as the foundation for solving BIEs corresponding to Laplace's equation. Accordingly, we focused on problems defined on \tilde{C}^2 -surfaces, which are common in IgA. Our theoretical

(a)



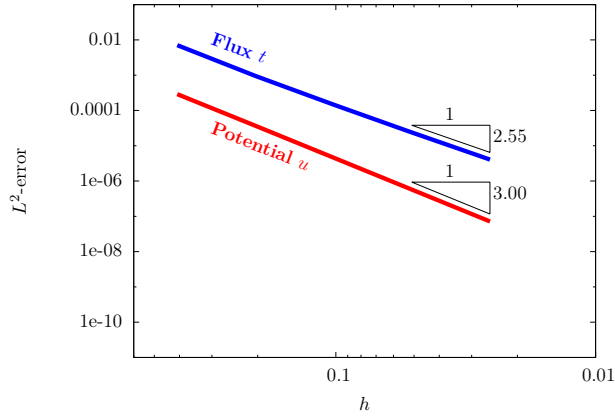
h	Flux		Potential	
	L^2 -error	eoc	L^2 -error	eoc
2.87E-01	2.62E-03		3.45E-04	
1.51E-01	2.58E-04	3.59	3.45E-05	3.57
7.73E-02	5.49E-05	2.32	5.93E-06	2.64
3.90E-02	5.77E-06	3.30	6.26E-07	3.29
1.96E-02	6.83E-07	3.08	7.47E-08	3.07

(b)



h	Flux		Potential	
	L^2 -error	eoc	L^2 -error	eoc
3.54E-01	1.04E-02		1.20E-03	
2.10E-01	1.11E-03	4.31	1.15E-04	4.51
1.09E-01	1.94E-04	2.66	2.18E-05	2.54
5.53E-02	1.99E-05	3.34	2.17E-06	3.38
2.77E-02	2.37E-06	3.08	2.55E-07	3.10

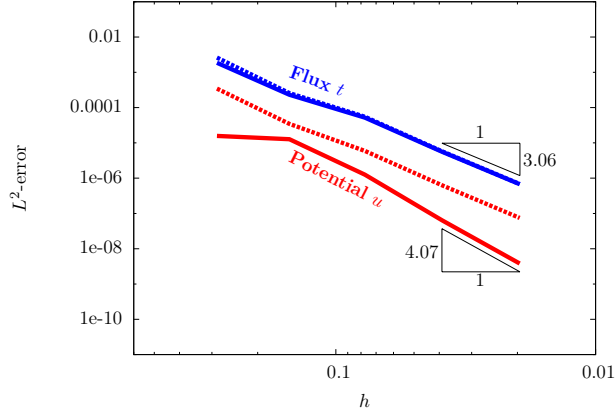
(c)



h	Flux		Potential	
	L^2 -error	eoc	L^2 -error	eoc
4.08E-01	7.08E-03		2.90E-04	
2.04E-01	9.54E-04	2.89	3.69E-05	2.98
1.02E-01	1.46E-04	2.70	4.59E-06	3.01
5.10E-02	2.38E-05	2.62	5.73E-07	3.00
2.55E-02	4.05E-06	2.55	7.16E-08	3.00

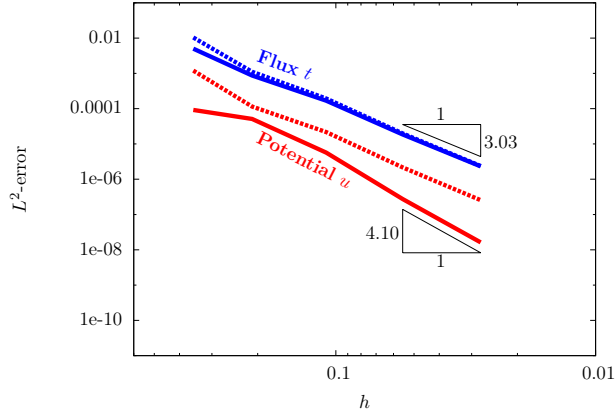
Figure 13: $L^2(\Gamma)$ -errors for the flux t and potential u on the (a) torus (b) sphere, and (c) cube. The approximations involved continuous basis functions degree $p = 2$ for u and discontinuous basis functions of degree $p = 2$ for t .

(a)



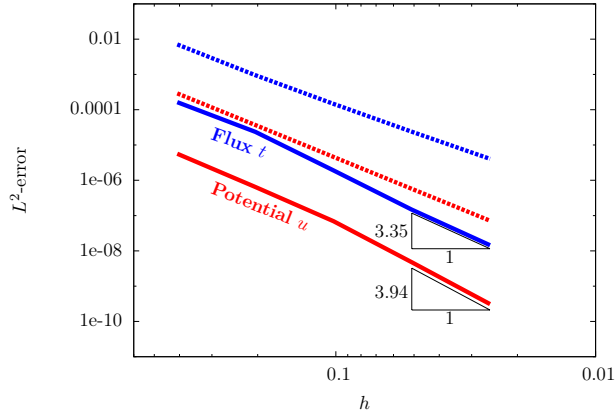
h	Flux		Potential	
	L^2 -error	eoc	L^2 -error	eoc
2.87E-01	1.87E-03		1.58E-05	
1.51E-01	2.32E-04	3.23	1.27E-05	0.33
7.73E-02	5.20E-05	2.25	1.26E-06	3.47
3.90E-02	5.59E-06	3.26	6.39E-08	4.36
1.96E-02	6.75E-07	3.06	3.82E-09	4.07

(b)



h	Flux		Potential	
	L^2 -error	eoc	L^2 -error	eoc
3.54E-01	5.03E-03		9.22E-05	
2.10E-01	8.67E-04	3.38	5.12E-05	1.13
1.09E-01	1.69E-04	2.51	5.68E-06	3.36
5.53E-02	1.86E-05	3.23	2.74E-07	4.45
2.77E-02	2.32E-06	3.02	1.62E-08	4.09

(c)



h	Flux		Potential	
	L^2 -error	eoc	L^2 -error	eoc
4.08E-01	1.64E-04		5.66E-06	
2.04E-01	2.35E-05	2.81	6.46E-07	3.13
1.02E-01	1.90E-06	3.63	6.91E-08	3.22
5.10E-02	1.47E-07	3.69	4.75E-09	3.86
2.55E-02	1.44E-08	3.35	3.10E-10	3.94

Figure 14: $L^2(\Gamma)$ -errors for the flux t and potential u on the (a) torus (b) sphere, and (c) cube. The approximations involved continuous basis functions degree $p = 3$ for u and discontinuous basis functions of degree $p = 2$ for t (solid lines). The dashed lines correspond to the results presented in Figure 13.

results and numerical schemes take full advantage of this geometric smoothness. In this regard, our work is a major departure from previous papers concerned with applying IgA to BIEs, where IgA was considered merely as a BEM with different basis functions.

Numerical schemes developed in this work allow one to apply collocation schemes to both SBIE and HSBIE; ordinarily the HSBIE can be analyzed within Galerkin’s setting only. The access to both SBIE and HSBIE was exploited for constructing governing linear algebraic equations with optimal spectral properties. Furthermore, all integral operators involved in the SBIE and HSBIE were reduced to weakly-singular integrals, for which we adopted effective numerical integration schemes available in the literature, including the polar coordinates transformation, local reparametrization of the surface, and recursive subdivision. This combination resulted in an exponentially convergent integration scheme, essential for attaining optimal approximation properties.

Adopting IgA for numerical treatment of BIEs necessitated the introduction of the following numerical schemes:

- Discontinuous basis functions for treating edges and vertices of non-smooth domains, and irregularities associated with collapsed edges and extraordinary points, both common in IgA.
- Local reparametrization of surfaces necessary for effective and accurate integration schemes, especially in the vicinity of collapsed edges.
- Degree elevated basis functions advantageous for solving mixed boundary-value problems.

There are several open issues, whose resolution may significantly advance IgA of BIEs. Among them are:

- Mathematical foundations for collocation schemes for BIEs corresponding to pure BVPs defined on non-smooth domains.
- Mathematical foundations for collocation schemes for BIEs corresponding to mixed BVPs defined on smooth and ultimately non-smooth domains.
- Efficient integration schemes for Galerkin discretizations.
- Better numerical integration schemes that exploit smoothness of the basis functions.
- Adaptive numerical integration and approximation schemes, in the spirit of $h - p - k$ methods, introduced and described herein [24, 25].

In conclusion, let us mention that most of the theoretical results and computational numerical schemes can be extended to equations of linear elasticity and Stokes equations of fluid mechanics. Those extensions may have a significant impact on the development of tools for engineering design and analysis.

8 Acknowledgement

T.J.R. Hughes was supported by grants from the Office of Naval Research (N00014-08-1-0992), the National Science Foundation (CMMI-01101007), and SINTEF (UTA10-000374) with the University of Texas at Austin. M. Taus was partially supported by a Fulbright fellowship, a NIMS graduate fellowships, and the National Science Foundation (CMMI-01101007). We thank these organizations for their generous support. We are also grateful to Professor Michael Scott (Brigham Young University) for sharing his code and helping with various implementation issues.

References

- [1] I. Akkerman, Y. Bazilevs, V. M. Calo, T. J. R. Hughes, and S. Hulshoff. The role of continuity in residual-based variational multiscale modeling of turbulence. *Computational Mechanics*, 41(3):371–378, 2008.
- [2] K. E. Atkinson and I. G. Graham. Iterative solution of linear systems arising from the boundary integral method. *SIAM journal on scientific and statistical computing*, 13(3):694–722, 1992.
- [3] F. Auricchio, L. Beirão da Veiga, A. Buffa, C. Lovadina, A. Reali, and G. Sangalli. A fully locking-free isogeometric approach for plane linear elasticity problems: A stream function formulation. *Computer Methods in Applied Mechanics and Engineering*, 197(14):160 – 172, 2007.
- [4] F. Auricchio, L. Beirão Da Veiga, T. J. R. Hughes, A. Reali, and G. Sangalli. Isogeometric collocation methods. *Mathematical Models and Methods in Applied Sciences*, 20(11):2075–2107, 2010.
- [5] F. Auricchio, L. Beirão da Veiga, C. Lovadina, and A. Reali. The importance of the exact satisfaction of the incompressibility constraint in nonlinear elasticity: mixed FEMs versus NURBS-based approximations. *Computer Methods in Applied Mechanics and Engineering*, 199(58):314 – 323, 2010.
- [6] F. Auricchio, L. Beiro da Veiga, T.J.R. Hughes, A. Reali, and G. Sangalli. Isogeometric collocation for elastostatics and explicit dynamics. *Computer Methods in Applied Mechanics and Engineering*, 249252(0):2 – 14, 2012.
- [7] Y. Bazilevs and I. Akkerman. Large eddy simulation of turbulent Taylor-Couette flow using isogeometric analysis and the residual-based variational multiscale method. *Journal of Computational Physics*, 229(9):3402 – 3414, 2010.
- [8] Y. Bazilevs, V. M. Calo, J. A. Cottrell, T. J. R. Hughes, A. Reali, and G. Scovazzi. Variational multiscale residual-based turbulence modeling for large eddy simulation of incompressible flows. *Computer Methods in Applied Mechanics and Engineering*, 197(14):173 – 201, 2007.
- [9] Y. Bazilevs, V. M. Calo, T. J. R. Hughes, and Y. Zhang. Isogeometric fluid-structure interaction: theory, algorithms, and computations. *Computational Mechanics*, 43(1):3–37, 2008.
- [10] Y. Bazilevs, V. M. Calo, Y. Zhang, and T. J. R. Hughes. Isogeometric Fluid-structure Interaction Analysis with Applications to Arterial Blood Flow. *Computational Mechanics*, 38(4-5):310–322, 2006.
- [11] Y. Bazilevs, J. R. Gohean, T. J. R. Hughes, R. D. Moser, and Y. Zhang. Patient-specific isogeometric fluid-structure interaction analysis of thoracic aortic blood flow due to implantation of the Jarvik 2000 left ventricular assist device. *Computer Methods in Applied Mechanics and Engineering*, 198(4546):3534 – 3550, 2009.
- [12] Y. Bazilevs, C. Michler, V. M. Calo, and T. J. R. Hughes. Isogeometric variational multiscale modeling of wall-bounded turbulent flows with weakly enforced boundary conditions on unstretched meshes. *Computer Methods in Applied Mechanics and Engineering*, 199(1316):780 – 790, 2010.
- [13] K. Belibassakis, T. Gerostathis, K. Kostas, C. Politis, P. Kaklis, A. Ginnis, and C. Feurer. A bem-isogeometric method with application to the wavemaking resistance problem of ships at constant speed. In *30th International Conference on Offshore Mechanics and Arctic Engineering, OMAE2011, Rotterdam, The Netherlands*, pages 95–102, 2011.
- [14] K. A. Belibassakis, T. P. Gerostathis, K. V. Kostas, C. G. Politis, P. D. Kaklis, A. I. Ginnis, and C. Feurer. A BEM-isogeometric method for the ship wave-resistance problem. *Ocean Engineering*, 60(0):53 – 67, 2013.
- [15] D. J. Benson, Y. Bazilevs, M.-C. Hsu, and T. J. R. Hughes. Isogeometric shell analysis: The Reissner-Mindlin shell. *Computer Methods in Applied Mechanics and Engineering*, 199(58):276 – 289, 2010.

- [16] D. J. Benson, Y. Bazilevs, M.-C. Hsu, and T. J. R. Hughes. A large deformation, rotation-free, isogeometric shell. *Computer Methods in Applied Mechanics and Engineering*, 200(1316):1367 – 1378, 2011.
- [17] M. J. Borden, C. V. Verhoosel, M. A. Scott, T. J. R. Hughes, and C. M. Landis. A phase-field description of dynamic brittle fracture. *Computer Methods in Applied Mechanics and Engineering*, 217220(0):77 – 95, 2012.
- [18] A. Böttcher, S.G. Mikhlin, R. Lehmann, and S. Pröbldorf. *Singular Integral Operators*. 2. Springer Berlin Heidelberg, 1987.
- [19] J. Bremer and Z. Gimbutas. A Nyström method for weakly singular integral operators on surfaces. *J. Comput. Phys.*, 231(14):4885–4903, 2012.
- [20] A. Buffa, G. Sangalli, and R. Vázquez. Isogeometric analysis in electromagnetics: B-splines approximation. *Computer Methods in Applied Mechanics and Engineering*, 199(1720):1143 – 1152, 2010.
- [21] E. Catmull and J. Clark. Recursively generated b-spline surfaces on arbitrary topological meshes. *Computer-aided design*, 10(6):350–355, 1978.
- [22] F. Cirak, M. Ortiz, and P. Schroder. Subdivision surfaces: a new paradigm for thin-shell finite-element analysis. *International Journal for Numerical Methods in Engineering*, 47(12):2039–2072, 2000.
- [23] F. Cirak, M. J. Scott, E. K. Antonsson, M. Ortiz, and P. Schröder. Integrated modeling, finite-element analysis, and engineering design for thin-shell structures using subdivision. *Computer-Aided Design*, 34(2):137–148, 2002.
- [24] J. A. Cottrell, T. J. R. Hughes, and Y. Bazilevs. *Isogeometric analysis: Toward Integration of CAD and FEA*. Wiley, Chichester, 2009.
- [25] J. A. Cottrell, T. J. R. Hughes, and A. Reali. Studies of refinement and continuity in isogeometric structural analysis. *Computer Methods in Applied Mechanics and Engineering*, 196(4144):4160 – 4183, 2007.
- [26] J. A. Cottrell, A. Reali, Y. Bazilevs, and T. J. R. Hughes. Isogeometric analysis of structural vibrations. *Computer Methods in Applied Mechanics and Engineering*, 195(4143):5257 – 5296, 2006.
- [27] D. J. Benson and Y. Bazilevs and E. De Luycker and M.-C. Hsu and M. Scott and T. J. R. Hughes and T. Belytschko. A generalized finite element formulation for arbitrary basis functions: From isogeometric analysis to xfem. *International Journal for Numerical Methods in Engineering*, 83(6):765–785, 2010.
- [28] R. Echter and M. Bischoff. Numerical efficiency, locking and unlocking of NURBS finite elements. *Computer Methods in Applied Mechanics and Engineering*, 199(58):374 – 382, 2010.
- [29] T. Elguedj, Y. Bazilevs, V. M. Calo, and T. J. R. Hughes. \bar{B} and \bar{F} projection methods for nearly incompressible linear and non-linear elasticity and plasticity using higher-order NURBS elements. *Computer Methods in Applied Mechanics and Engineering*, 197(3340):2732 – 2762, 2008.
- [30] G. Folland. *Introduction to partial differential equations*. Princeton University Press, 1995.
- [31] A. I. Ginnis, C. Feurer, K. A. Belibassakis, P. D. Kaklis, K. V. Kostas, T. P. Gerostathis, and C. G. Politis. A Catia ship-parametric model for isogeometric hull optimization with respect to wave resistance. In *ICCAS 2011*. Royal Institution of Naval Architects, 2011.
- [32] H. Gómez, V. M. Calo, Y. Bazilevs, and T. J. R. Hughes. Isogeometric analysis of the Cahn-Hilliard phase-field model. *Computer Methods in Applied Mechanics and Engineering*, 197(4950):4333 – 4352, 2008.
- [33] H. Gómez, T. J. R. Hughes, X. Nogueira, and V. M. Calo. Isogeometric analysis of the isothermal Navier-Stokes-Korteweg equations. *Computer Methods in Applied Mechanics and Engineering*, 199(2528):1828 – 1840, 2010.

- [34] G. G. C. Hsiao and W. W. L. Wendland. *Boundary Integral Equations*. Applied Mathematical Sciences Series. Springer-Verlag Berlin Heidelberg, 2008.
- [35] T. J. R. Hughes, J. A. Cottrell, and Y. Bazilevs. Isogeometric analysis: CAD, finite elements, NURBS, exact geometry and mesh refinement. *Computer Methods in Applied Mechanics and Engineering*, 194(3941):4135 – 4195, 2005.
- [36] K. H. Muci-Küchler and T. J. Rudolphi. A weakly singular formulation of traction and tangent derivative boundary integral equations in three dimensional elasticity. *Engineering Analysis with Boundary Elements*, 11(3):195 – 201, 1993.
- [37] J. Kiendl, Y. Bazilevs, M.-C. Hsu, R. Wüchner, and K.-U. Bletzinger. The bending strip method for isogeometric analysis of Kirchhoff-Love shell structures comprised of multiple patches. *Computer Methods in Applied Mechanics and Engineering*, 199(3740):2403 – 2416, 2010.
- [38] Kang L. and Xiaoping Q. Isogeometric analysis and shape optimization via boundary integral. *Computer Aided Design*, 43(11):1427–1437, 2011.
- [39] S. Lipton, J. A. Evans, Y. Bazilevs, T. Elguedj, and T. J. R. Hughes. Robustness of isogeometric structural discretizations under severe mesh distortion. *Computer Methods in Applied Mechanics and Engineering*, 199(58):357 – 373, 2010.
- [40] A. P. Nagy, M. M. Abdalla, and Z. Gürdal. Isogeometric sizing and shape optimisation of beam structures . *Computer Methods in Applied Mechanics and Engineering*, 199(1720):1216 – 1230, 2010.
- [41] A. P. Nagy, M. M. Abdalla, and Z. Gürdal. On the variational formulation of stress constraints in isogeometric design . *Computer Methods in Applied Mechanics and Engineering*, 199(4144):2687 – 2696, 2010.
- [42] M. J. Peake, J. Trevelyan, and G. Coates. Extended isogeometric boundary element method (XIBEM) for two-dimensional Helmholtz problems. *Computer Methods in Applied Mechanics and Engineering*, 259(0):93 – 102, 2013.
- [43] L. Piegl and W. Tiller. The nurbs book. 1997. *Monographs in Visual Communication*, 1997.
- [44] C. Politis, A. I. Ginnis, P. D. Kaklis, K. Belibassakis, and C. Feurer. An isogeometric BEM for exterior potential-flow problems in the plane. In *2009 SIAM/ACM Joint Conference on Geometric and Physical Modeling*, pages 349–354. ACM, 2009.
- [45] Xiaoping Q. Full analytical sensitivities in NURBS based isogeometric shape optimization. *Computer Methods in Applied Mechanics and Engineering*, 199(2932):2059 – 2071, 2010.
- [46] D. F. Rogers. *An introduction to NURBS: with historical perspective*. Elsevier, 2000.
- [47] Y. Saad and M. H. Schultz. GMRES: A Generalized Minimal Residual Algorithm for Solving Nonsymmetric Linear Systems. *SIAM J. Sci. Stat. Comput.*, 7(3):856–869, 1986.
- [48] M. Sabin. Recent progress in subdivision: a survey. In *Advances in Multiresolution for Geometric Modelling*, pages 203–230. Springer, 2005.
- [49] S. A. Sauter and C. Schwab. Boundary Element Methods. In *Boundary Element Methods*, volume 39 of *Springer Series in Computational Mathematics*, pages 183–287. Springer Berlin Heidelberg, 2011.
- [50] D. Schillinger, L. Dedè, M. A. Scott, J. A. Evans, M. J. Borden, E. Rank, and T. J. R. Hughes. An isogeometric design-through-analysis methodology based on adaptive hierarchical refinement of NURBS, immersed boundary methods, and T-spline CAD surfaces. *Computer Methods in Applied Mechanics and Engineering*, 249252(0):116 – 150, 2012.
- [51] P. Schröder, D. Zorin, T. DeRose, D. R. Forsey, L. Kobbelt, M. Lounsbery, and J. Peters. Subdivision for modeling and animation. *ACM SIGGRAPH Course Notes*, 12, 1998.

- [52] C. Schwab and W. L. Wendland. On numerical cubatures of singular surface integrals in boundary element methods. *Numerische Mathematik*, 62(1):343–369, 1992.
- [53] M. A. Scott. *T-splines as a Design-Through-Analysis Technology*. PhD thesis, The University of Texas at Austin, 2011.
- [54] M. A. Scott, R. N. Simpson, J. A. Evans, S. Lipton, S. P. A. Bordas, T. J. R. Hughes, and T. W. Sederberg. Isogeometric boundary element analysis using unstructured T-splines. *Computer Methods in Applied Mechanics and Engineering*, 254(0):197 – 221, 2013.
- [55] T. W. Sederberg, J. Zheng, A. Bakenov, and A. Nasri. T-splines and t-nurccs. In *ACM transactions on graphics (TOG)*, volume 22, pages 477–484, 2003.
- [56] R. N. Simpson, S. P. A. Bordas, J. Trevelyan, and T. Rabczuk. A two-dimensional isogeometric boundary element method for elastostatic analysis. *Computer Methods in Applied Mechanics and Engineering*, 209-212:87–100, 2012.
- [57] R. N. Simpson, M.A. Scott, M. Taus, D.C. Thomas, and H. Lian. Acoustic isogeometric boundary element analysis. *Computer Methods in Applied Mechanics and Engineering*, 269(0):265 – 290, 2014.
- [58] O. Steinbach. *Numerical Approximation Methods for Elliptic Boundary Value Problems: Finite and Boundary Elements*. Texts in applied mathematics. Springer, 2008.
- [59] W. A. Wall, M. A. Frenzel, and C. Cyron. Isogeometric structural shape optimization. *Computer Methods in Applied Mechanics and Engineering*, 197(3340):2976 – 2988, 2008.
- [60] Y. Zhang, Y. Bazilevs, S. Goswami, C. L. Bajaj, and T. J. R. Hughes. Patient-specific vascular NURBS modeling for isogeometric analysis of blood flow. *Computer Methods in Applied Mechanics and Engineering*, 196(2930):2943 – 2959, 2007.

A Compactness of double-layer operators on C^2 -surfaces

In this section we prove that the double-layer operators \mathcal{K} and \mathcal{K}' defined on $\Gamma \in C^2$ are compact operators on the space of continuous functions.

Consider a bounded domain $\Omega \subset \mathbb{R}^3$ with $\Gamma := \partial\Omega$. By definition $\Gamma \in C^2$ if it satisfies the following conditions:

1. For any $x \in \Gamma$ there exists a constant $R > 0$, independent of x , and a neighborhood $N_x \subset \mathbb{R}^3$ such that $\text{dist}(x, \Gamma \setminus N_x) > R$;
2. The surface $\Gamma_x := \Gamma \cap N_x$ is an image of a domain $\hat{N}_x \subset \mathbb{R}^2$ under the map ψ_x ;
3. The map ψ_x is bijective and twice continuously differentiable;
4. The maps ψ_x and ψ_x^{-1} are Lipschitz continuous.

Theorem A.1. *If $\Gamma \in C^2$ then there exists a constant $C > 0$ such that*

$$\left| \frac{(x - y) \cdot n(y)}{4\pi|x - y|^3} \right| \leq \frac{C}{|x - y|}$$

for all $x, y \in \Gamma$.

Proof. Let $x \in \Gamma$. If $y \notin \Gamma_x$, then there exists a constant $R > 0$ such that $\text{dist}(x, \Gamma \setminus \Gamma_x) > R$ and consequently $|y - x| > R$. As a result we obtain the estimate

$$\left| \frac{(x - y) \cdot n(y)}{4\pi|x - y|^3} \right| \leq \frac{\text{diam}(\Omega)}{4\pi R^3} \leq \frac{\text{diam}(\Omega)^2}{4\pi R^3} \frac{1}{|x - y|}.$$

If $y \in \Gamma_x$ then there exist $\hat{x} \in \hat{N}_x$ and $\hat{y} \in \hat{N}_x$ such that $\psi_x(\hat{x}) = x$ and $\psi_x(\hat{y}) = y$ because ψ_x is bijective. Since ψ_x is twice continuously differentiable, we can use the following expressions for the normal

$$n(y) = \frac{\frac{\partial \psi_x(\hat{y})}{\partial \hat{y}_1} \times \frac{\partial \psi_x(\hat{y})}{\partial \hat{y}_2}}{\left| \frac{\partial \psi_x(\hat{y})}{\partial \hat{y}_1} \times \frac{\partial \psi_x(\hat{y})}{\partial \hat{y}_2} \right|}$$

and Taylor's expansion

$$x - y = \psi_x(\hat{x}) - \psi_x(\hat{y}) = \frac{\partial \psi_x(\hat{y})}{\partial \hat{y}_1}(\hat{x}_1 - \hat{y}_1) + \frac{\partial \psi_x(\hat{y})}{\partial \hat{y}_2}(\hat{x}_2 - \hat{y}_2) + \mathcal{O}(|\hat{x} - \hat{y}|^2)$$

to obtain the estimate

$$(x - y) \cdot n(y) = \mathcal{O}(|\hat{x} - \hat{y}|^2).$$

Since ψ_x^{-1} is Lipschitz continuous, there exists a constant $l > 0$ such that $l|\hat{x} - \hat{y}| \leq |\psi_x(\hat{x}) - \psi_x(\hat{y})| = |x - y|$, which implies

$$\left| \frac{(x - y) \cdot n(y)}{4\pi|x - y|^3} \right| = \mathcal{O}\left(\frac{1}{|x - y|}\right).$$

□

This theorem implies that the operator \mathcal{K} is weakly singular. Similarly, we can establish the bound

$$\left| \frac{(x - y) \cdot n(x)}{4\pi|x - y|^3} \right| \leq \frac{C}{|x - y|} \quad \forall x, y \in \Gamma,$$

and thus establish that the operator \mathcal{K}' is also weakly singular.

Using well-established techniques, it can be proved that the operators $\mathcal{K}, \mathcal{K}' : C(\Gamma) \rightarrow C(\Gamma)$ are compact and the operators $\frac{1}{2}I + \mathcal{K}$ and $\frac{1}{2}I - \mathcal{K}'$ are invertible [30, Chapter 3]. Furthermore, if we assume that there exists a bounded interpolation operator that maps continuous functions onto continuous basis functions (24), one can invoke compact perturbations theory to prove that the discrete problems (18) and (20) are uniquely solvable and their solutions \tilde{u}_h and \tilde{t}_h satisfy quasi-optimal error estimates in the $L^\infty(\Gamma)$ -norm [18, Chapter XII.1].